

## Photometric anomalies of the lunar surface studied with SMART-1 AMIE data

V. Kaydash <sup>a,\*</sup>, M. Kreslavsky <sup>b</sup>, Yu. Shkuratov <sup>a</sup>, S. Gerasimenko <sup>a</sup>, P. Pinet <sup>c</sup>, J.-L. Josset <sup>d</sup>, S. Beauvivre <sup>d</sup>, B. Foing <sup>e</sup>, and the AMIE SMART-1 Team

<sup>a</sup> Astronomical Institute of Kharkov National University, Sumskaya 35, Kharkov 61022, Ukraine

<sup>b</sup> Earth and Planetary Sciences, University of California - Santa Cruz, 1156 High St., Santa Cruz, CA 95064, USA

<sup>c</sup> UMR 5562/CNRS/Toulouse III University, OMP (Midi-Pyrenees Observatory), 14 Av. E. Belin, 31400 Toulouse, France

<sup>d</sup> Space Exploration Institute, Case postale, CH-2002 Neuchâtel, Switzerland

<sup>e</sup> ESA/ESTEC, Keplerlaan 1, 2201 Noordwijk, The Netherlands

### ARTICLE INFO

#### Article history:

Received 31 October 2008

Revised 12 March 2009

Accepted 15 March 2009

Available online 19 March 2009

#### Keywords:

Moon, surface

Photometry

Cratering

Regoliths

### ABSTRACT

We present new results from the mapping of lunar photometric function parameters using images acquired by the spacecraft SMART-1 (European Space Agency). The source data for selected lunar areas imaged by the AMIE camera of SMART-1 and the data processing are described. We interpret the behavior of photometric function in terms of lunar regolith properties. Our study reveals photometric anomalies on both small (sub-kilometer) and large (tens of kilometers) scales. We found the regolith mesoscale roughness of lunar swirls to be similar in Mare Marginis, Mare Ingenii, and the surrounding terrains. Unique photometric properties related to peculiarities of the millimeter-scale regolith structure for the Reiner Gamma swirl are confirmed. We identified several impact craters of subkilometer sizes as the source of photometric anomalies created by an increase in mesoscale roughness within the proximal crater ejecta zones. The extended ray systems reveal differences in the photometric properties between proximal and distant ejecta blankets. Basaltic lava flows within Mare Imbrium and Oceanus Procellarum indicate higher regolith porosity for the redder soils due to differences in the chemical composition of lavas.

© 2009 Elsevier Inc. All rights reserved.

## 1. Introduction

The observable optical properties of the lunar surface are formed in the uppermost layers of the regolith. The interaction of light with the regolith includes several physical phenomena such as single scattering, incoherent multiple scattering between particles, mutual shadowing of particles, coherent multiple backscatter enhancement at opposition, and effects of macroscopic roughness (e.g., Hapke, 1993). For given illumination/observation geometry, the relative contribution of all those effects is controlled by the physical properties of the regolith, such as the transparency of regolith particles, the shape and compaction of them, everything that governs the regolith structure at different scales from comparable to the wavelength of the incident light to the spatial resolution of observations. Therefore, observable variations of photometric properties contain some information about the regolith structure.

To describe the bidirectional reflectance variations  $R$  on the lunar surface at arbitrary observation/illumination geometry, the photometric function  $F$ , given by  $R(i, \varepsilon, \varphi) = R_0 F(i, \varepsilon, \varphi)$ , is used. In this equation  $i$  is the incidence angle,  $\varepsilon$  is the emission or view-

ing angle,  $\varphi$  is the azimuth angle (the angle between the plane of incidence and the plane of emergence), and  $R_0$  is the reflectivity determined at a specific angle geometry, e.g.,  $R_0 = R(0, 0, 0)$  (e.g., Hapke, 1993). For some applications another set of angles (photometric coordinates) are more convenient to use: the photometric longitude  $\gamma$ , the photometric latitude  $\beta$ , and the phase angle  $\alpha$ . For the Earth-based observations of the Moon at large or moderate phase angles,  $\beta$ ,  $\gamma$  are close to the selenographic latitude and longitude. The relationships between  $(i, \varepsilon, \varphi)$  and  $(\alpha, \beta, \gamma)$  are (e.g., Hapke, 1993):

$$\left. \begin{aligned} \cos \alpha &= \cos \varepsilon \cos i + \sin \varepsilon \sin i \cos \varphi \\ \cos \gamma &= \cos \varepsilon / \cos \beta \\ \cos \beta &= \sqrt{\frac{(\sin(i+\varepsilon))^2 - (\cos \frac{\varphi}{2})^2 \sin 2\varepsilon \sin 2i}{(\sin(i+\varepsilon))^2 - (\cos \frac{\varphi}{2})^2 \sin 2\varepsilon \sin 2i + (\sin \varepsilon)^2 (\sin i)^2 (\sin \varphi)^2}} \end{aligned} \right\} \quad (1)$$

and

$$\left. \begin{aligned} \cos i &= \cos \beta \cos(\gamma - \alpha) \\ \cos \varepsilon &= \cos \beta \cos \gamma \\ \cos \varphi &= \frac{\cos \alpha - \cos i \cos \varepsilon}{\sin i \sin \varepsilon} \end{aligned} \right\}. \quad (2)$$

The dependence of the photometric function  $F$  on the photometric coordinates can be presented as follows (e.g., Hapke, 1993):  $F(\alpha, \beta, \gamma) = f(\alpha) \cdot D(\alpha, \beta, \gamma)$ , where  $f(\alpha)$  is the phase function

\* Corresponding author.

E-mail address: vkgaydash@gmail.com (V. Kaydash).

and  $D(\alpha, \beta, \gamma)$  is the disk function. For observations from a long distance the phase function is responsible for the phase angle dependence of brightness of surface sites independently of their position on the apparent disk, while the disk function describes the brightness distribution over the apparent disk at a given phase angle. For observations from a spacecraft orbiting the Moon, Eqs. (1) and (2) operate with topocentric coordinates  $\varepsilon$  and  $\alpha$ . For the nadir looking geometry often used in orbital surveys, the photometric angles  $\beta \approx \gamma \approx 0$ , whereas for spot pointing (or target tracking) geometry those angles vary significantly. The photometric angles  $(\alpha, \beta, \gamma)$  for the observer on the lunar orbit retain the properties of photometric coordinates. Factorization of the photometric function into disk and phase functions is convenient and often used, although it is formal and has no theoretical basis. The idea of such a factorization is based on the following considerations. Intrinsic properties of a given lunar site do not depend on its position on the apparent lunar disk, while the apparent brightness does. The disk function accounts for this dependence. The remaining term, the phase function, can be considered as the surface brightness recalculated to a standard position on the apparent disk; it could be used to derive intrinsic properties of the lunar surface.

The mapping of the phase function is a promising way to study lunar surface processes. The detailed studies of the lunar phase function began many years ago (Barabashev, 1922; Fedorets, 1952; van Diggelen, 1964; Gehrels et al., 1964). The strong backscatter of light from the Moon in a wide range of phase angles was discovered by Barabashev (1922) with the photographic photometry. Gehrels et al. (1964) were the first to establish the term “opposition effect of the Moon” (a nonlinear increase in brightness when the phase angle approaches zero, dubbed also “opposition spike”) as a phenomenon, which is separate from the general backscattering property of the lunar surface and possibly has a different explanation. Later, development of imaging techniques allowed the mapping of lunar phase function parameters with telescopic observations. Works by Wildey (1978) and Akimov and Shkuratov (1981) were the pioneering studies of phase ratio method which eliminates the albedo variations on the phase ratio image (i.e. the ratio of images obtained at different phase angles) thus allows extracting the information on photometric function itself. A phase angle ratio image of the Moon  $f(2.0^\circ)/f(4.5^\circ)$  has been obtained by Wildey (1978) who mapped the ratio with low resolution. Mapping of the phase angle ratio  $f(3.2^\circ)/f(14.5^\circ)$  at two wavelengths has been performed by Akimov and Shkuratov (1981). They found that lunar sites with moderate albedo (bright mare or dark highlands) show the maximal steepness of brightness phase function in the studied phase angle range. Then several phase ratio maps  $f(1^\circ)/f(16^\circ)$ ,  $f(6^\circ)/f(12^\circ)$ , and  $f(12^\circ)/f(96^\circ)$  have been obtained by Shkuratov et al. (1994). By analysis of these phase ratios, the authors found anomalies of regional distribution of opposition spike parameters; those anomalies indicated mare areas of different age and composition. It has been shown that regional variations of the phase angle ratios can be attributed to variations of albedo and roughness of the lunar surface (Akimov and Shkuratov, 1981; Shkuratov et al., 1994).

The Clementine mission (Nozette et al., 1994) has stimulated quantitative studies of lunar photometric properties with high resolution. In particular, the opposition effect of selected lunar areas using Clementine images has been studied (Buratti et al., 1996; Shkuratov et al., 1999; Kreslavsky et al., 2000). It has been found that the amplitude of the opposition surge depends on both the wavelength and the terrain type. Shkuratov et al. (1999) and Kreslavsky et al. (2000) concluded that the spike parameters are controlled by small-scale surface structure and proposed to detect variations of lunar regolith properties (porosity and roughness) by the opposition spike measurements. They also noted that some

areas associated with the Reiner Gamma swirl show unusual photometric behavior, indicating that this feature is smoother than the typical mare regolith at small scales. Several photometric anomalies imaged by Clementine have been carefully studied and discussed in terms of regolith characteristics by Kreslavsky and Shkuratov (2003), who have noted a general anticorrelation between phase function steepness and albedo. They suggested the increase of single-particle albedo would enhance the illumination of the shadowed areas in regolith layer with diffusely scattered light; in this way it weakens the shadow hiding effect and thus decreases the phase function steepness. They also have found several sites imaged in the Clementine survey with noticeable departures from this tendency. In particular, among photometric anomalies, they have found anomalous halos around small impact craters and the Apollo 15 landing site and anomalies related to increased surface roughness. A similar technique has been applied to the imaging data of High Resolution Stereo Camera onboard Mars Express by Kreslavsky et al. (2006). They showed that maps of photometric anomalies give interpretable information about the martian surface structure. For example, less steep phase function of floors of some craters and rimless depressions filled with wind-blown material indicated the absence of pebbles and rock fragments. Recent results produced with the use of Hapke modeling showed that these anomalies could be interpreted in physical terms involving variations related to the nature of the powder particulate surface (i.e., packing/compression/narrow size distribution) (Pinet et al., 2006; Pinet et al., 2008; Jehl et al., 2008). This shows that the present procedure is relevant for the mapping of surface variations in the regolith structure.

Recently some photometric results obtained with SMART-1 (Small Missions for Advanced Research in Technology) data have been published in Muinonen et al. (2009), Foing et al. (2008), Chevrel et al. (2008) and Souchon et al. (2009). Photometric analysis of 220 lunar images obtained by SMART-1 led Muinonen et al. (2009) to the conclusion that the lunar mare opposition effect is caused by coherent backscattering and single scattering at the scales of lunar particles sizes; whereas contribution of shadow-hiding to opposition effect is very small. The major role of the coherent backscatter mechanism in narrow opposition spike was also noted in previous works (e.g., Shkuratov et al., 1999). Foing et al. (2008) presented lunar North and South poles photometric mosaics at typical 300 m/pixel resolution. The optical response of pyroclastic deposits has also been documented by means of AMIE dedicated spot-pointing observations (Chevrel et al., 2008; Souchon et al., 2009). We present here new results of the mapping of photometric function parameters using the lunar images recently acquired by SMART-1 and interpret the behavior of the photometric function in terms of lunar regolith properties.

## 2. Data, their processing and key for interpretation

### 2.1. The AMIE camera and data set

SMART-1, the first mission of European Space Agency to visit the Moon, was launched from Kourou on 27 September 2003 (Foing et al., 2006). Among several instruments carried by SMART-1, the AMIE (Advanced Moon micro-Imager Experiment) camera was the onboard imaging system of the mission. The AMIE camera detector was a CCD ( $1024 \times 1024$  pixels in size, dynamic range of 1023 DN) with three color filters (centered at 750, 915, and 960 nm) and one wideband filter; all filters were placed directly onto the detector surface. The wideband or “no-filter” area size was  $512 \times 512$  pixels, i.e. 1/4 of the total detector area. The signal-to-noise ratio was higher for the no-filter area than for the color-filter ones. The aperture and focal length of AMIE optics gave the angular resolution of

$0.00576^\circ/\text{pixel}$  or  $46 \text{ m/pixel}$  at  $500 \text{ km}$  altitude (Pinet et al., 2005; Josset et al., 2006). During the lunar orbit phase of the SMART-1 mission (December 2004–August 2005) about 13,000 images of the lunar surface were acquired with the AMIE camera, and in the extended mission phase (October 2005–August 2006)  $\sim 19,000$  additional images were obtained. The baseline SMART-1 lunar orbit was highly elliptical with a perilune between 300 and 700 km close to the lunar South Pole. This orbit allowed a spatial resolution of the AMIE imaging from tens of meters at the high and mid southern latitudes to hundreds of meters at the equator and low/mid northern latitudes. The major part of the SMART-1 survey was performed in a nadir-looking mode, i.e. with the viewing angle  $\varepsilon$  close to zero. During spot-pointing (or “target-tracking”) campaigns, several lunar sites were successively imaged under constant Sun illumination, but varying viewing angle  $\varepsilon$ , while the spacecraft moved along its orbit. Overlapping images taken at different observation or illumination geometry give a potential possibility to determine parameters of the phase function and to search for photometric anomalies (Pinet et al., 2005).

## 2.2. Image calibration

The preliminary pipeline calibration of the AMIE data (Koschny et al., 2003) accounts for the removal of flat-field and dark current properties as a function of exposure time and detector temperature. It has been shown that the preliminary calibration gives reasonable results (Cerroni et al., 2006). Later the careful analysis (Grieger, 2007) of in-flight data revealed a significant change in the dark current after the long ( $\sim 18$  months) cruise phase of the mission, before the lunar encounter, therefore the pipeline calibration of AMIE data has been updated. The up-to-date procedure for AMIE calibration (Grieger, 2008) has the following improvements: new master dark frames have been computed from dark sky observations; a new flat field has been estimated from the in-flight data. The calibration includes the following steps: (a) implementing the function for the focal plane temperature dependence of the dark current using master bias and master dark frames, (b) applying the in-flight flat field. We also perform two additional normalizations of calibrated frames: (1) division to exposure duration and (2) multiplication by the second power of distance between the Sun and the Moon at the time of frame acquisition. In such a way we get digital numbers of pixels, which are proportional to the bidirectional reflectance, and the proportionality coefficients, though unknown, are supposed to be the same for all frames taken with the AMIE camera.

No absolute calibration has been performed so far (Grieger, 2008). Fortunately, using the above described procedure, we are able to work with the pixel values proportional to the brightness, which enables us to produce phase-ratio images and look for photometric anomalies. Since the color-filter parts of each image have much lower signal-to-noise ratio and are adversely affected by stray light from the adjacent no-filter CCD area, we deal only with the no-filter subframes.

For the photometric analysis, images of the same scene obtained at different observation geometries are spatially transformed into a common projection using the latest version of AMIE SPICE kernels (Dougnac and Beauvivre, 2008). This SPICE information is based on the reconstructed knowledge of the spacecraft position, orientation, and time of image acquisition, which allows us to calculate the selenographic coordinates for each pixel in the frames as well as photometric coordinates  $(\alpha, \beta, \gamma)$ . After map-projecting the images using these SPICE kernels, the residual miss-registration of images  $<0.1^\circ$  in longitude/latitude was observed. This can be explained by small errors in the knowledge of AMIE boresight orientation and the curvature of the field of view. We performed the final coregistration of overlapping images at a

subpixel accuracy by a “rubber sheet” geometric transformation: necessary local shifts were found by maximizing local correlation between images. The formal accuracy of the coregistration algorithm that we developed is  $1/10$  pixel. The coregistration accuracy benefits from the fact that the point-spread function of AMIE detector is almost equal to 1 pixel (Koschny et al., 2003), i.e. the smallest resolvable detail in the AMIE images would occupy 1 pixel. With this, the ratios of co-registered images give perfectly sensitive and reliable test of co-registration quality.

## 2.3. Approximation of the lunar photometric function

The quantitative description of photometric properties of the Moon requires an approximation of the observed photometric function  $F$  with an analytical function having a small number of free parameters. In such a way we may express variations in the photometric properties as variations in the analytical function parameters. The quantity of small phase angle ( $<10^\circ$ ) images in the AMIE survey is extremely small, i.e. there are very few images containing the opposition spike (Kaydash et al., 2008). This allows us to use a simple phase function  $f(\alpha)$  to approximate AMIE measurements and not to take into account the non-linearity at small phase angles. We use an empirical formula proposed by Akimov (1979), because it provides a very good approximation of lunar photometric data. This function has been successfully applied to Clementine data (Kreslavsky et al., 2000; Kreslavsky and Shkuratov, 2003). At  $\alpha > 10^\circ$  Akimov’s approximation expresses the photometric function through the photometric angles  $\alpha$ ,  $\beta$ , and  $\gamma$  as follows:

$$F(\alpha, \beta, \gamma) = \exp(-\eta\alpha) \cos \frac{\alpha}{2} \frac{(\cos^{q+1}(\gamma - \frac{\alpha}{2}) \sin^{q+1} \frac{\alpha}{2})}{\cos \gamma (1 - \sin^{q+1} \frac{\alpha}{2})} \cos^q \beta. \quad (3)$$

The first multiplier is the phase function  $\exp(-\eta\alpha)$  dependent solely on the phase angle  $\alpha$ ; the second one is the disk function describing in our case the orientation of the scattering surface with respect to the Sun and the observer for a given  $\alpha$ . This formula contains only two adjustable parameters, the parameter of the disk function  $q$  and the steepness of phase function,  $\eta$ . The disk function in formula (3) being empirical has Lambert law as a limit case at  $q = 1$ , whereas at  $q = 0$  it is very similar to Lommel–Seeliger law (Akimov and Shkuratov, 1981; Akimov, 1988a). There is a theoretical expression for the special case of Akimov’s disk function, which does not contain any free parameter (Akimov, 1975). This parameter-free function was derived from the formal condition that a surface being randomly undulated should have the same disk function as before undulations (the case of “extremely rough” surface). This function also can be derived for fractal-like surfaces (e.g., Shkuratov et al., 1999). Note the disk function in Eq. (3) is similar to parameter-free Akimov’s function when  $q = 2$ . The Moon has a rough surface in a global scale, i.e. it is neither flat nor “extremely rough”. Thus formula (3) is suitable for the photometric description of surfaces with intermediate values of roughness. So here  $q$  has the sense of global roughness of the Moon as a planet and variations of parameter  $q$  should reflect changes of global roughness (Akimov, 1988a).

The phase function in a simple exponential form  $\exp(-\eta\alpha)$  was suggested to describe the shadow-hiding effect on the phase function (Akimov, 1988b). The coefficient  $\eta$  takes into account diminution of the shadow-hiding effect due to multiple scattering (Shkuratov et al., 1999). Specifically,  $\eta$  characterizes shadowing by surface roughness and depends on surface structure.

Using these considerations we apply description (3) to SMART-1 data in order to map and analyze the photometric function parameters.

**Table 1**

Parameters of SMART-1 AMIE images used in the current photometric study.

Lunar site studied	Fig.	Orbit/frame number	Center longitude (deg)	Center latitude (deg)	Incidence angle (deg)	Emission angle (deg)	Phase angle (deg)	Scale (m/pix)
Gruithuisen domes	2, 3	2236/8	−39.52	35.84	45.07	29.85	68.80	159.4
		2236/9	−39.52	35.83	45.10	14.15	55.84	134.4
		2236/10	−39.52	35.83	45.13	3.71	42.49	117.9
		2236/11	−39.52	35.83	45.15	18.10	34.10	111.3
		2236/12	−39.52	35.82	45.15	29.88	30.26	109.5
Crater Lavoisier	6, 7	2251/7–2251/37	−80.77	38.19	45	0–45	27–80	111–200
Mare Marginis	9	603/15	87.3	16.65	16.86	24.52	9.43	128.4
		79/70	86.37	16.75	58.52	2.32	59.94	186.4
Mare Ingenii	10	142/40	165.13	−35.72	81.45	1.84	82.61	117.6
		2871/16	166.04	−35.82	68.39	38.76	106.83	137.1
Reiner Gamma	11, 12	1781/41	−57.77	8.04	57.55	2.21	56.38	147
		1918/6	−57.32	7.46	70.88	27.83	98.47	168.5
		2243/7	−59.53	7.23	28.99	1.62	30	79.2
		2110/12	−58.84	7.96	52.72	8.4	61.06	93.2
		2110/13	−58.79	6.44	52.63	8.34	60.93	91.4
Crater Louise	13	518/9	−34.58	29.46	33.59	1.91	34.76	171.7
		635/14	−34.09	29.07	28.06	26.13	17.6	142.5
Olbers A ray system	14	40/64	−68.28	16.92	43.76	23.04	43.21	214.1
		114/76	−68.79	15.91	69.81	2.25	71.32	198.9
Crater Lichtenberg	15, 16	40/85	−66.43	32.95	49.86	20.3	44.34	261.3
		114/94	−67.54	33.72	72.01	2.6	73.73	250
		530/9	−67.06	34.14	36.59	2.22	38.02	179.8
		2110/9	−68.40	33.79	52.29	23.25	73.84	138.2
Lomonosov floor	17	469/9	97.92	28.0	38.12	2.16	39.5	175.2
		2319/10	97.94	28.15	32.4	17.36	15.31	93.9
Mare Serenitatis	18	2214/11	21.40	18.25	39.41	2.87	36.56	95.7
		2082/1	21.05	18.05	62.93	5.79	64.36	113.6
		2082/2	21.04	18.07	62.93	2.8	63.72	111.5
		2082/3	21.03	18.09	62.93	0.41	63.13	109.6
Western Procellarum near Briggs	19	40/75	−67.42	25.15	46.45	21.7	42.96	236.4
		114/86	−68.20	25.24	70.74	2.42	72.36	224.3
North–West of Mare Imbrium	20	105/98	−27.45	39.39	71	2.74	72.79	265.6
		516/9	−28.77	39.03	42.15	2.07	43.4	190.8

#### 2.4. Mapping the phase function steepness with spot-pointing observations

In principle, for the spot-pointing observations, when we have three or more images of the same place obtained from different directions, we can simultaneously estimate both parameters of the photometric function approximation (3),  $\eta$  and  $q$ , as has been done in Kreslavsky et al. (2000), Kreslavsky and Shkuratov (2003). The Clementine spot-pointing observations used in those works contain images obtained with similar phase angles  $\alpha$  and different emission angles  $\varepsilon$  (the phase angle has a minimum in the series of the spot-pointing images, in other words, the trajectory of the observation geometry formed a loop in the  $\alpha - \varepsilon$  domain), which allowed independent fit of the disc function and phase function parameters. For the set of SMART-1/AMIE observations, the phase angle does not have a minimum,  $\alpha$  changes monotonically in accord with the emission angle (no loop in the  $\alpha - \varepsilon$  domain, see, e.g., Section 3.3, observation conditions), and the two parameters are poorly deconvolvable. All we can do is to assume some reasonable value of  $q$  and then derive  $\eta$  from the observations. For this purpose we applied a least square fit procedure to find the parameter of phase function  $\eta$  in Eq. (3) by minimizing the following sum:

$$\sum_{i=1}^N [R_i/R_0 - F(\alpha_i, \beta_i, \gamma_i, q, \eta)]^2 \rightarrow \min, \quad (4)$$

where  $N$  is the number of independent measurements of the bidirectional reflectance  $R_i$  at different viewing geometries  $\alpha_i$ ,  $\beta_i$ ,  $\gamma_i$ .

In this paper we study the photometric properties of the flat (mainly mare) areas. Similar flat mare areas were particularly studied in (Kreslavsky et al., 2000; Kreslavsky and Shkuratov, 2003). They found for mare surfaces the disk function parameter  $q$  varies in the range 0.1–0.5 and has little effect on the pattern of derived  $\eta$ . For a set of lunar sites they performed least square fitting procedure for simultaneous derivation  $(q, \eta)$  and found  $q \approx 0.3$  as the best fit value. We also ran the fit procedure several times for different values of  $q$  from 0.1–0.5 range and confirmed that obtained  $\eta$  is rather insensitive to variations of assumed  $q$ . We finally adopted  $q = 0.3$  for this study. Note that the disk function is a very smooth function; it does not have sharp local extrema within a single AMIE image. Due to this, a bias in assumed  $q$  mainly affects the absolute values of  $\eta$  for all the pixels in the whole image independently on their position in the image. Therefore we can readily compare values of  $\eta$  across the image searching for the local peculiarities of the phase function steepness, even if our guess of  $q$  is not perfect.

Images in the spot-pointing series significantly differ in resolution, up to a factor of two (e.g., see column “Scale” in Table 1 for Gruithuisen domes and crater Lavoisier). This introduces additional error into the phase function steepness estimates. To get rid of this error we convolved images in the series with a proper Gaussian kernel to reduce their resolution to the lowest resolution in the series. This procedure eliminates artifacts caused by the res-

olution difference, however, it results in a decrease of the overall map resolution.

We should note that the local photometric angles  $\alpha$ ,  $\beta$ , and  $\gamma$  were calculated from SPICE kernels assuming that the surface is an ideal sphere. Surface tilts (i.e. surface topography), which are not negligible at the typical resolution of lunar SMART-1 imagery (~100–200 m/pix, can disturb the values of local photometric angles. Therefore, our approach is presently valid for flat areas only (mare, smooth plains, crater floors, etc.). Thus, the analysis is only possible for scenes that contain at least some flat areas.

## 2.5. Mapping the phase function steepness from phase ratios

The total number of suitable spot-pointing observations is rather limited. The SMART-1 data set gives another possibility to study photometric behavior of the lunar surface. Some areas were imaged twice in the regular survey from different orbits, thus providing data for phase ratio mapping. In this paper we present several new examples of phase ratio images and analyze them in terms of the regolith structure.

Following the definition of photometric function  $F(\alpha, \beta, \gamma) = f(\alpha) \cdot D(\alpha, \beta, \gamma)$  and using the approximation (3) we can calculate the parameter  $\eta$  from the phase ratio images  $R_1/R_2$  as follows:

$$\eta = \frac{\ln\left(\frac{R_1}{R_2} \frac{D(\alpha_2, \beta_2, \gamma_2)}{D(\alpha_1, \beta_1, \gamma_1)}\right)}{\alpha_2 - \alpha_1}. \quad (5)$$

Unlike the case of spot-pointing observations, the illumination direction differs between the images making the pair, hence, the locations of geometric shadows at the surface are different, which increases the amount of “false” objects at the derived maps of parameter  $\eta$ . In addition, for the spot-pointing observations, the procedure of  $\eta$  estimation implicitly involved averaging of a number of images thus reducing noise; this is not the case for the phase ratios. Thus, the least square fit procedure (4) is more accurate than the calculation by formula (5). The more points on this curve we have the more accurate estimation of  $\eta$  we get. The extreme case is the use of only two points in the curve for the estimation of the steepness. In this case we draw a line (in the reflectance logarithm vs. phase angle plot) between two points, which is actually expressed by Eq. (5). The  $\eta$  parameter is sensitive to different scales of regolith structure at different ranges of  $\alpha$  (see Section 2.6 for details). Thus, the comparison of the absolute  $\eta$  values obtained for very different phase angles range should be performed with caution because in that case we deal with separate parts of phase curve affected by different effects of light scattering. For example, the lunar opposition spike at low phase angle range  $\alpha \leq 4^\circ$  is characterized by nonlinear (even in logarithmic scale) increase of brightness when  $\alpha$  approaches zero (e.g., Shkuratov et al., 1999). Thus, formally derived  $\eta$  value for a low  $\alpha$  should be greater than for a moderate  $\alpha$ .

## 2.6. Key for result interpretation

We noted in the introduction that the photometric behavior of the regolith surface is controlled by several interrelated physical effects: single-particle scattering, incoherent multiple scattering (light diffusion between particles), shadow hiding effect, coherent backscatter enhancement, and macroscopic surface roughness. Generally, the steepness of phase function is affected by all these factors that act at a wide range of scales from the wavelength to resolution of the image (e.g., Hapke, 1993; Shkuratov et al., 1999; Cord et al., 2005; Cord et al., 2007).

Albedo can also affect  $\eta$  in the following way: growth of the single-particle albedo leads to the surface albedo enhancement,

thus the illumination of the shadowed areas with diffusely scattered light is also growing. In this way the shadow hiding effect weakens and thereby  $\eta$  is also decreases (e.g., Hapke, 1986, 1993). As a result albedo-related variations of the phase function steepness are characterized by inverse correlation between  $\eta$  and albedo.

For different ranges of angle  $\alpha$ , different scales of the regolith structure affect the phase curve behavior. For the smallest phase angles  $\alpha \leq 4^\circ$ , bright surfaces produce the coherent enhancement of backscattering (e.g., Shkuratov et al., 1999). The spatial scale responsible for such an effect is on the order of tens of wavelengths of the incident light. We, however, do not consider small phase angles in this paper.

At larger phase angles  $\alpha \sim 40$ –50° the phase function is mainly affected by the shadow-hiding effect and incoherent multiple scattering which are developed on the surface structures comparable to typical sizes of regolith particles (~100 µm) (Hapke, 1993; Shkuratov et al., 2005). In this  $\alpha$  range, the inverse dependence of the phase function steepness on the surface albedo is usually observed; this dependence is caused by partial illumination of shadowed areas due to semitransparency of regolith particles.

At  $\alpha > 40$ –50° the regolith surface topography (from submillimeter size up to spatial resolution of the imaging system used) noticeably affects the phase function and plays a key role (Shkuratov et al., 2005; Cord et al., 2003, 2005). For rather dark surfaces, the steepness of phase function is almost independent of albedo at large  $\alpha$ . Thus, the spatial distribution of phase function parameters could reveal the information on peculiarities of the lunar regolith structure at different scales.

How does the phase ratio or the phase function slope (measured from remote-sensing photometry) relate to quantitative parameters (porosity, roughness, volume density, etc.) of the real lunar surface structure? The answer would rely on a combination of orbital photometry with *in situ* measurements of the regolith microstructure at the Moon. The only *in situ* data available are the microphotographs of the lunar surface taken by the astronauts of the Apollo expeditions (e.g., Gold, 1971). The structure of the uppermost layer of the regolith being altered by space weathering processes, mostly probably, the micrometeorite bombardment, cannot be preserved when the lunar samples are delivered to a laboratory. By the quantitative photogrammetric study of the stereomicrophotographs of the lunar surface, Helfenstein and Shepard (1999) showed that the undisturbed soil at Apollo-14 landing site is rougher at all scales from 0.1 mm to centimeters than the undisturbed soil at Apollo-11 and -12 sites. One of the explanations for this phenomenon is the blowing of the soil by gases from the jet engine of the lander during the landing: the microphotographs at the Apollo-14 landing site were taken at a distance of 180 m from the lander, while the microphotographs at the Apollo-11 and -12 landing sites were taken at a much smaller distance (Helfenstein and Shepard, 1999). On the other hand, the mapping of the phase function slope distribution for the vicinity of the Apollo-15 landing site by Kreslavsky and Shkuratov (2003) have revealed a photometric anomaly, which coincides with landing site. They have interpreted this feature (seen as a low- $\eta$  spot, i.e. representing flatter phase function) as the lunar soil disturbed by the impact of gas jets from the lunar module engine. The authors reported the following quantities regarding optical properties of the landing site: disk function parameter, averaged over the landing site vicinity,  $q = 0.28 \pm 0.05$ , phase function steepness  $\eta = 0.66$  for the landing site,  $\eta = 0.75$  for its vicinity. Using these estimates we can suggest that damage of the regolith structure at mm–cm scale can decrease  $\eta$  values by 10–20%. One feature of increased  $\eta$  (the phase function is ~20% steeper in comparison to the surroundings) was found by Kreslavsky and Shkuratov (2003). The increase of  $\eta$  would be related to peculiarities of the regolith source material or to increased

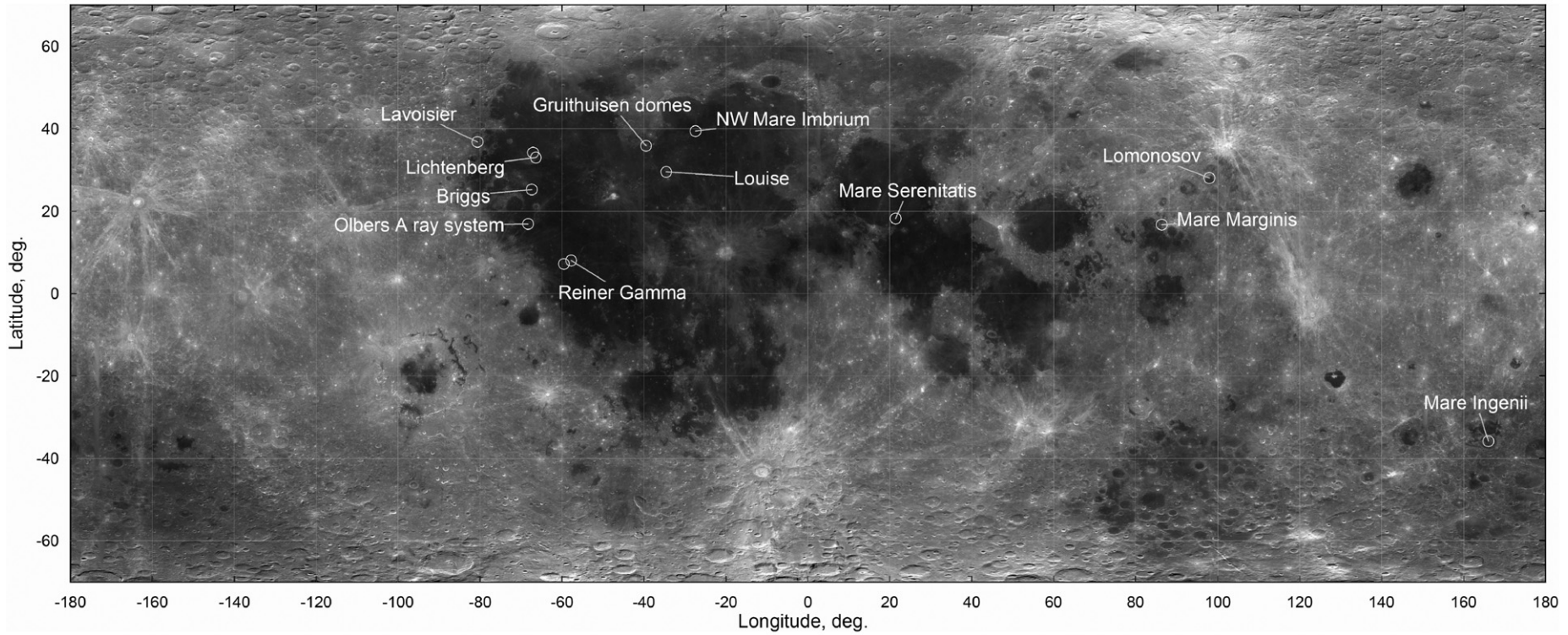


**Fig. 1.** Locations of all sites studied in this work. Background: Clementine albedo basemap in simple cylindrical projection.

large-scale surface roughness, e.g., due to the presence of excessive number of boulders on the surface (e.g., Shkuratov and Helfenstein, 2001).

We note again that we can reliably estimate the phase function steepness only if scene is flat, i.e. it has no measurable topography at the spatial resolution of the data used. The topography of the surface at scales smaller than the spatial resolution contributes to the photometric behavior and is the object of our study.

### 3. Multiangular photometry

In this section we present our maps of the phase function steepness and main types of features observed in these maps; the next section is devoted to interpretation of these observations. Table 1 lists all sites considered, numbers of relevant figures in this paper, selenographic coordinates, AMIE images used, their resolution, and the illumination/observation conditions. Images are identified as "SMART-1 orbit number"/"AMIE frame number within orbit". Fig. 1 shows locations of the sites on a global lunar map. We start with results of spot-pointing observations (multiangular photometry), then describe results obtained from the phase ratio images.

#### 3.1. Gruithuisen domes

The area centered at  $39.5^{\circ}$  W,  $35.8^{\circ}$  N includes Gruithuisen domes and surrounding mare in the western part of Mare Imbrium. Five successive images were obtained in the SMART-1 orbit 2236 using the spot-pointing mode (see Table 1). The time lag between subsequent images varied from 3 to 7 min. We calibrated each image in the given set using the procedure described above. Small time difference between frames and the same exposure time of 10 ms reduces the effect of possible instability of camera parameters. Fig. 2a presents the nadir viewing SMART-1 image 2236/10 transformed into the Mercator projection, North is up. We use this projection for all lunar images presented in this paper.

The flat topped Gruithuisen  $\delta$  dome is seen just at the image center, the deep crater to the east from  $\delta$  dome is 9 km size Gruithuisen B, the northern flank of the Gruithuisen  $\zeta$  dome is seen at the bottom of the image as well as Gruithuisen  $\gamma$  at the left. The domes are proposed to be of volcanic origin of Imbrian period (e.g., Chevrel et al., 1999 and references therein).

We derived a map of the parameter  $\eta$  (Fig. 2b) using Eq. (4) for  $N = 5$ . Major apparent variations of the parameter  $\eta$  are associated with surface tilts (especially the  $\gamma$ ,  $\delta$ ,  $\zeta$  domes) and look like illuminated topography. Walls of resolved craters, ridges, pits are also seen as contrast black and white details and do not reflect real variations of the parameter  $\eta$ . As has been discussed, the estimate of  $\eta$  for these areas is not possible due to unknown actual illumination/observation geometry for the tilted facets. Thus, we may analyze flat areas only.

White arrows in Fig. 2b mark two compact bright objects with high  $\eta$  values ( $\sim 0.82$ – $0.83$ ). Black arrows mark two compact bright objects with diffuse extended halos of low  $\eta$  values ( $\sim 0.65$ – $0.70$ ). An enlarged view of this area is presented in Fig. 3 (one more low- $\eta$  feature is indicated by black arrow); it clearly shows that these halos are larger in size than the bright objects, thus the  $\eta$  anomalies here are not immediately caused by the albedo variations.

The patch of bright material lying at the toe of Gruithuisen  $\delta$  (marked with gray arrow) shows an inverse correlation between  $\eta$  and albedo: the brighter the surface, the gentler the phase function. We also note large-scale subtle variations of  $\eta$  over the mare surface (encircled area in Figs. 2b and 3b) characterized by somewhat lower  $\eta$  values (Kaydash et al., 2007a).

To check if there are distinguishable topography variations associated with the discussed features, we analyzed the high resolution

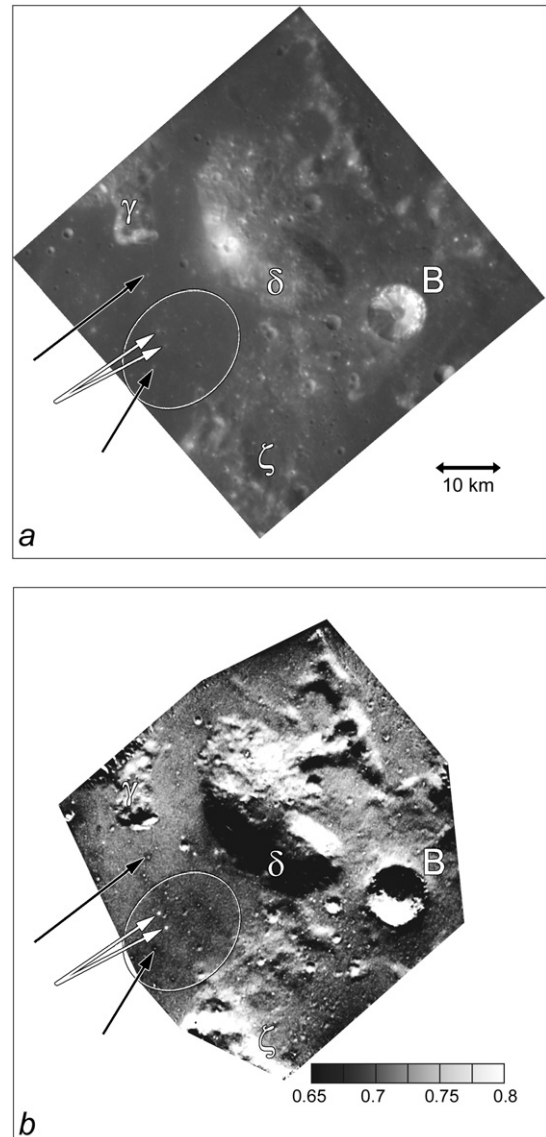


**Fig. 2.** Gruithuisen domes area: (a) reflectance, AMIE image 2236/10 at  $42^{\circ}$  phase angle; (b) a map of the phase function steepness  $\eta$  with a scale bar. Hereafter, brighter shades on the  $\eta$  maps denote steeper phase function. White arrows point to positive photometric anomalies associated with small craters. Black arrows point to negative photometric halos around some craters. Outlined area is an extended negative anomaly. Here and in all other images Mercator projection is used, north is up.

Lunar Orbiter (LO) image VHR\_5185 (available at <http://astrogeology.usgs.gov/Projects/LunarOrbiterDigitization/>) obtained under low Sun (Fig. 3c). This image reveals smooth wrinkle ridges extended to the south from Gruithuisen  $\gamma$  and between Gruithuisen  $\gamma$  and  $\delta$ . Visual inspection of the high resolution image for the two high- $\eta$  bright objects (white arrows) reveals the presence of  $\leq 200$  m crater inside one of them and a complex of three  $\leq 100$  m overlapping craters inside the other. In the centers of the three low- $\eta$  circular halos (black arrows) we also found small craters (in two cases) and a complex of several small craters (for the other case). The low- $\eta$  halos also are not linked to any distinguishable topography features. Therefore, the probable reason of the photometric variations here is the change of structure of the upper regolith layer.

As we noted in Section 2.6, the phase function steepness for moderate and large phase angles is controlled by the shadowing effect. For brighter surfaces, shadowed areas are better illuminated

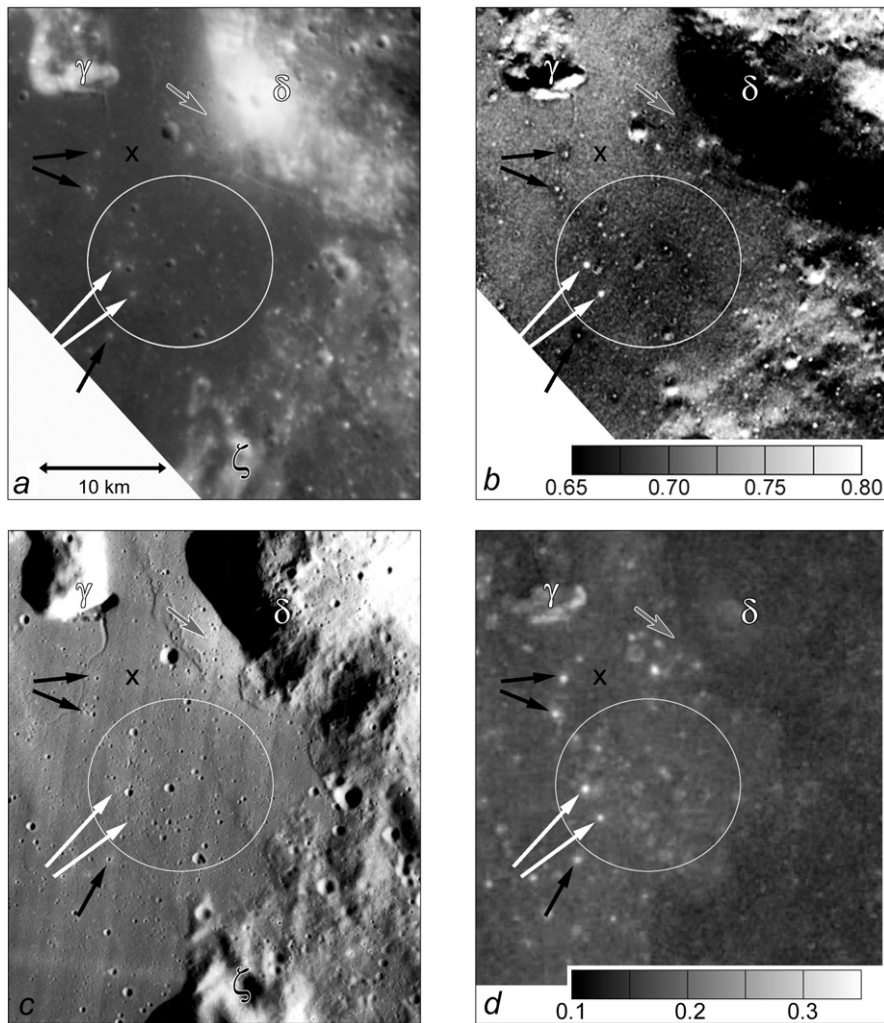


**Fig. 3.** Enlarged section of Fig. 2: (a) reflectance image at 42° phase; (b) phase function steepness  $\eta$ ; (c) high resolution LO V image VHR\_5185; (d) optical maturity parameter OMAT from Clementine data. Hereafter, darker shades on the OMAT maps denote lower OMAT values that correspond to more mature soils. White arrows point to positive photometric anomalies associated with small craters. Black arrows point to negative photometric halos around some craters. Gray arrow point to albedo-related low- $\eta$  feature at the toe of Gruithuisen  $\delta$ .

by diffusely scattered light and, therefore, the role of shadows is weaker. As a result, the phase function is gentler (i.e. less steep). Thus one should expect a general inverse correlation between the phase function steepness and albedo. Taking into account these considerations, we refer high- $\eta$  features which do not obey this reverse correlation rule as “positive” photometric anomalies and low- $\eta$  features that are not accompanied by higher albedo as “negative” photometric anomalies.

Large-scale subtle variations of  $\eta$  over the mare surface (outlined area in Figs. 2b, 3b, 3c and 3d) may be explained by the presence of more fine-grained material (pyroclastic?) in the vicinity of volcanic domes. Similar weak negative anomalies near volcanic edifices were observed both in Clementine data (Kreslavsky and Shkuratov, 2003) and in Earth-based maps of phase ratio  $f(12^\circ)/f(96^\circ)$  (Shkuratov et al., 1994). A map of the optical maturity index OMAT (Lucey et al., 2000b) (Fig. 3d) indicates the mare surface within domes triangle ( $\gamma$ ,  $\delta$ ,  $\zeta$ ) as an immature (increased OMAT) feature in comparison with the right part of the scene (e.g., Gruithuisen  $\delta$ ). Calculation the OMAT value over outlined area in Fig. 3 gives 0.19 (high-OMAT craters are excluded) while “typical mare” spot outside the ellipse (marked with “X”) has OMAT = 0.17. Formally, these estimations favor a hypothesis of the presence of less mature material in the outlined area, which is naturally accompanied by porosity variations. On the other hand, titanium

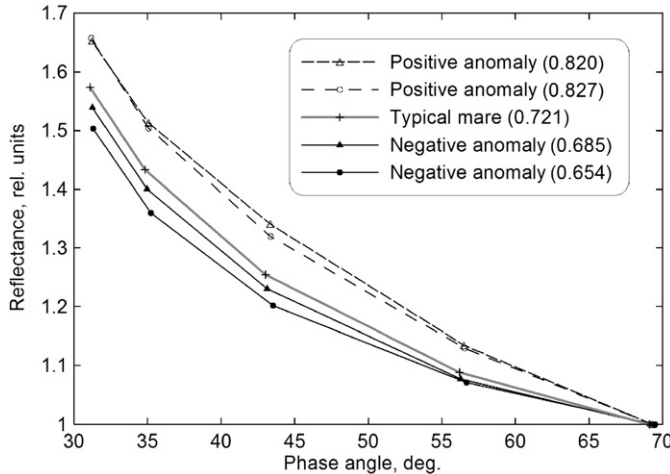
and iron maps, calculated for this area by method of Lucey et al. (2000a) do not display noticeable chemical composition differences from the neighborhood, as would be expected for distinctive pyroclastic deposits. An alternative explanation for such an area is that for a surface with low or moderate albedo, the shape of the single-particle indicatrix can contribute to the phase function of the surface directly, through single scattering. The shape of indicatrix is affected by the accumulation of the submicroscopic metallic iron due to space weathering (Hapke, 2001). In such a way subtle differences in OMAT values could be linked to variations of phase function steepness.

Fig. 4 shows brightness phase curves for selected sites in the Gruithuisen area indicated by arrows in Figs. 2 and 3. The curves are normalized at  $\alpha = 70^\circ$ . Values of  $\eta$  calculated by the least square fitting procedure (4) are shown in the upper inset in parentheses. Curves marked as “positive anomalies” in the inset correspond to high- $\eta$  crater halos indicated by white arrows in Figs. 2 and 3. Curves marked as “negative anomalies” correspond to the low- $\eta$  crater halo closest to the  $\gamma$  dome ( $\eta = 0.685$ ) and to the low- $\eta$  crater halo closest to the  $\zeta$  dome ( $\eta = 0.654$ ). The “typical mare” curve ( $\eta = 0.721$ ) corresponds to the spot marked by “X” in Fig. 3. So the highest- $\eta$  positive anomaly differs from the “typical mare” by  $\sim 15\%$  and lowest- $\eta$  negative anomaly differs from the “typical mare” by  $\sim 10\%$ .

### 3.2. Crater Lavoisier

Spot-pointing AMIE observations were carried out for the orbit 2251, when 33 images of a large (70 km) pre-Nectarian floor-fractured crater Lavoisier ( $80.8^\circ$  W,  $38.2^\circ$  N) were taken. Fig. 5 presents observation conditions for this series as a function of the frame number. Lavoisier was classified by Schultz (1976) as class III (wide floor moat) crater. According to that classification, class III craters commonly present volcanic vents (cones and fissures) and low albedo deposits. Wide fractures in those craters are typically filled by mare or light plains units (Schultz, 1976). The Lavoisier rim is largely eroded (Fig. 6a) and its maximal height is  $\sim 1.2$  km above the lowest point of the crater floor, according to the topography map from (Kaydash et al., 2007b). The local rise ( $\sim 200$ – $300$  m) near the center of crater Lavoisier carries two 5–6 km size craters. The southern one is double-ringed, indicating a layered structure of the Lavoisier floor. Dark spots mostly located at the periphery of crater floor do not reveal any prominent topography (Kaydash et al., 2007b).

As in the Gruithuisen case we cannot analyze tilted surface areas (Lavoisier rim, resolved walls of tectonic fractures, ridges, etc.) due to unknown local observation geometry. We note several



**Fig. 4.** Normalized brightness phase curves for selected sites in Gruithuisen area indicated by arrows in Figs. 2 and 3. “Positive anomaly” curves correspond to high- $\eta$  crater halos indicated by white arrows and “negative anomaly” curves correspond to low- $\eta$  crater halos indicated by black arrows. Values of  $\eta$  parameter calculated by Eq. (4) are shown in parentheses.

photometric features related to Lavoisier floor and small craters (Fig. 6b). The dark areas at the periphery of floor are not distinguishable at the  $\eta$  parameter map (cf. Fig. 6a), as we would anticipate from general anticorrelation between albedo and the phase function steepness. Note that 7 dark spots of  $3$ – $18$  km $^2$  area were identified as small pyroclastic deposits by Gaddis et al. (2003) (their original data are available from the Lunar Pyroclastic Volcanism Project at [http://astrogeology.usgs.gov/Projects/LunarPyroclastic Volcanism](http://astrogeology.usgs.gov/Projects/LunarPyroclasticVolcanism)). These deposits are titanium- and iron-enriched in comparison with crater floor and contain dark, glass-rich, friable materials (Gaddis et al., 2000). The dark spots may have smoother surface structure, which would compensate the effect of albedo on  $\eta$ , so that the dark deposits do not show up in the  $\eta$  map.

There is no common link between chemical differences in lunar soil and variations of surface roughness. However, some difference between highland and mare regolith has been noted by Engelhardt et al. (1976): plagioclase, which dominates the highland soil and rocks, can be crushed by micrometeorite impacts more efficiently than mafic minerals occurring in mare materials. Possibly there are other chemically different lunar materials which do not have the same fragility and may be characterized by a different roughness.

Lavoisier floor gave us two more examples of extended negatively anomalous halos around young small craters; they are shown with arrows 1 and 2 in Figs. 7a and 7b. The most puzzling feature is the large negative anomaly outlined by the circle around the two larger craters (4.6 and 5.6 km in size). Tectonic fractures across the floor are also crossing this feature though anomaly does not coincide with dark spots. On the other hand, visual inspection of all the 7 dark spots marked in Lunar Pyroclastic Volcanism Project as small pyroclastic deposits reveal that they directly coincide with fractures, which are likely to be volcanic vents (Schultz, 1976). Thus we believe that this low- $\eta$  feature might be caused by pyroclastic deposits associated with dark spots and tectonic fractures across the floor. The spectral signature of these proposed pyroclastic deposits, however, is very different form that of the 7 dark spots.

We show in Fig. 8 brightness phase curves normalized at  $\alpha = 70^\circ$  for two photometric anomalies pointed by arrows 1 and 2 in Fig. 7 and for the typical crater floor surface as well as values of  $\eta$  parameter calculated by the least square fitting procedure (4).

### 3.3. Phase ratios

Here we briefly present our results obtained with the phase ratio method. Our interpretation of these results is given in Section 4.

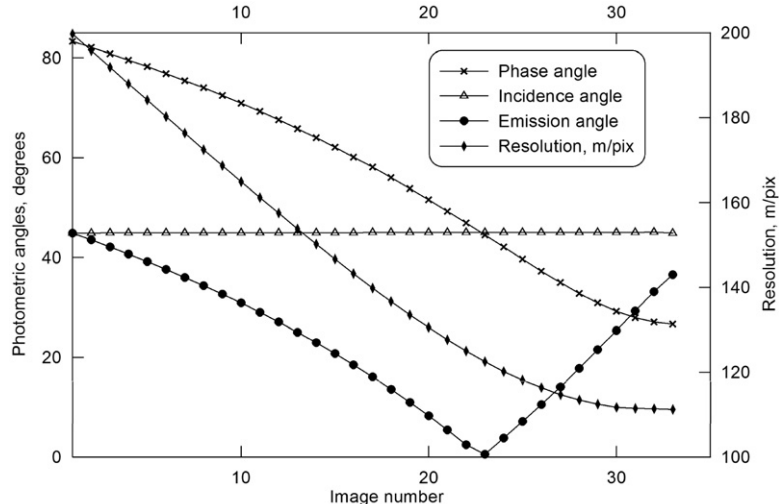


**Fig. 5.** Observation conditions for crater Lavoisier spot-pointing campaign at orbit 2251 as a function of the frame number.

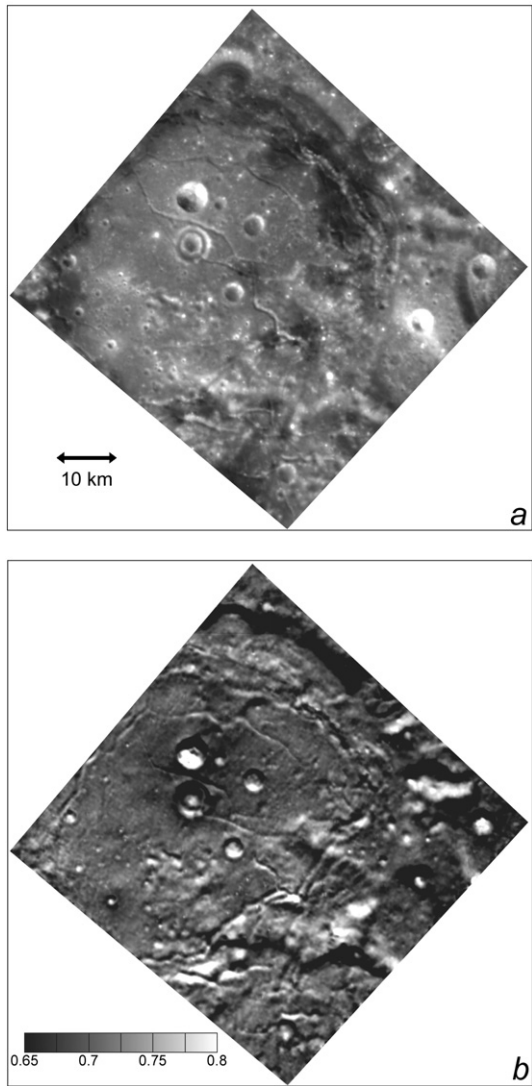


**Fig. 6.** Crater Lavoisier: (a) reflectance image at 45° phase (AMIE image 2251/27); (b) photometric function steepness  $\eta$  with a scale bar.

### 3.3.1. Mare Marginis

Lunar swirls, diffuse bright albedo features, are of exceptional interest for photometric studies; the AMIE data set gives a limited possibility to study a few of them. One of the locations is a part of the swirl in Mare Marginis. We took a pair of AMIE images, 79/70 and 603/15, covering an area of 60 × 60 km. Fig. 9a presents the larger-phase-angle (60°) image from the pair centered at 86.4° E, 16.8° N (see Table 1). The big crater (50 km) in the left part of the frame is Goddard C, the smaller one to the east is Goddard B (12 km). The most prominent examples of swirls are marked with black arrows. Our map of  $\eta$  (Fig. 9b) shows that the swirls are characterized by prominently low phase function steepness with 20% lower  $\eta$  values, than neighboring mare and highland areas. Since the phase angle difference between images in the pair is very wide (9.4° and 60°), a wide range of scales of the regolith structure (from micro- to meso-topography) affects the phase function steepness (see Section 2.6). Shadow lightening certainly contributes to the observed decrease of  $\eta$  in the bright swirls.

### 3.3.2. Mare Ingenii

The AMIE survey gave a unique opportunity to map steepness of the phase function at large phase angles for one sample of lunar

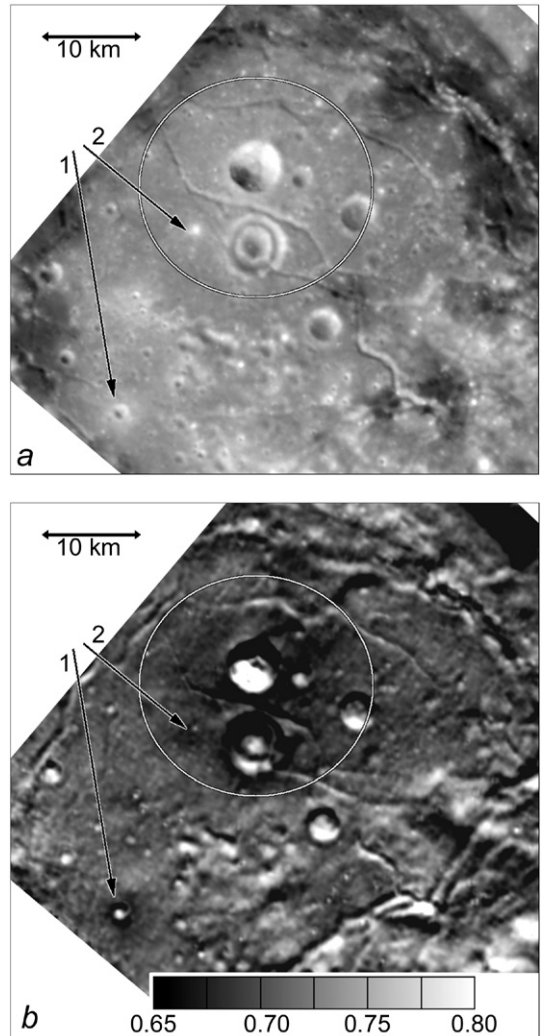


**Fig. 7.** Enlarged section of Fig. 6 in the central part of Lavoisier floor: (a) nadir-looking reflectance image; (b)  $\eta$  parameter map. Arrows point to the negative photometric halos around craters. Outlined area is a large negative anomaly in the center of Lavoisier floor.

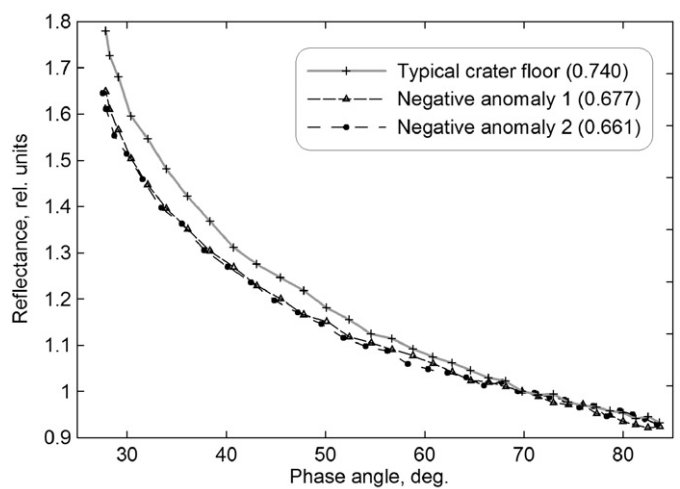


**Fig. 8.** Normalized brightness phase curves for two negative anomalies linked to craters pointed by arrows in Fig. 7 and regular area in Lavoisier floor. “Negative anomaly 1” curve corresponds to the feature pointed by arrow 1, “Negative anomaly 2” curve is for the area pointed by arrow 2 in Fig. 7. Values of  $\eta$  calculated with Eq. (4) are shown in parentheses.

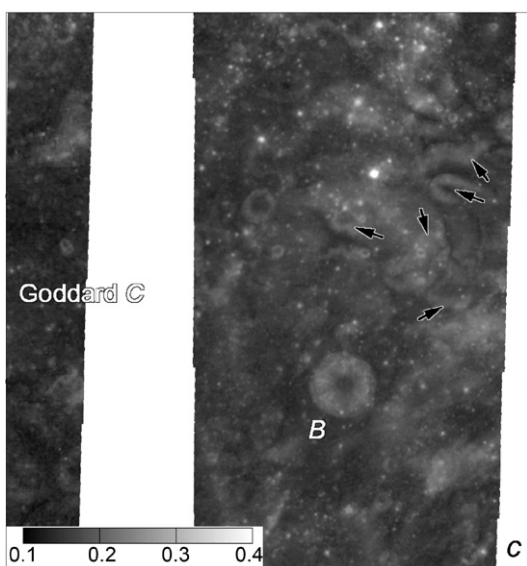
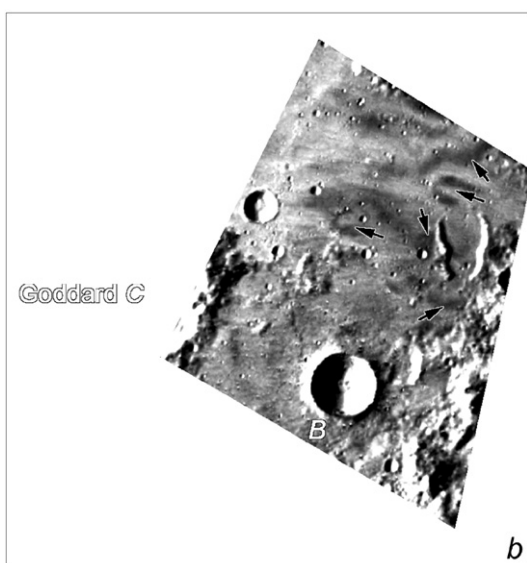
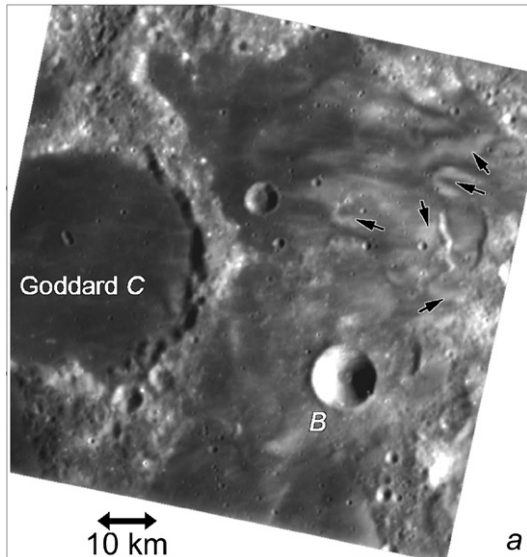


**Fig. 9.** Swirl in mare Marginis: (a) reflectance image at 60° phase (AMIE frame 79/70); (b) parameter of phase steepness  $\eta$  obtained from  $f(9.4^\circ)/f(60^\circ)$  phase ratio; (c) optical maturity parameter OMAT by Clementine data. Arrows point to swirl features with low  $\eta$  values.

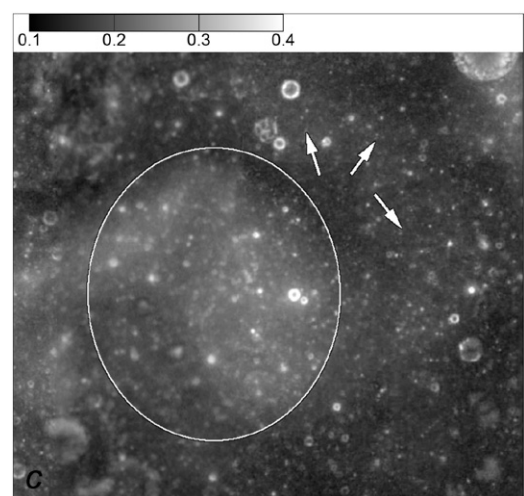
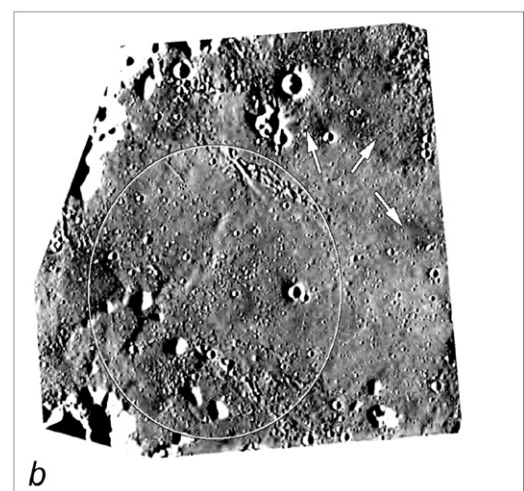
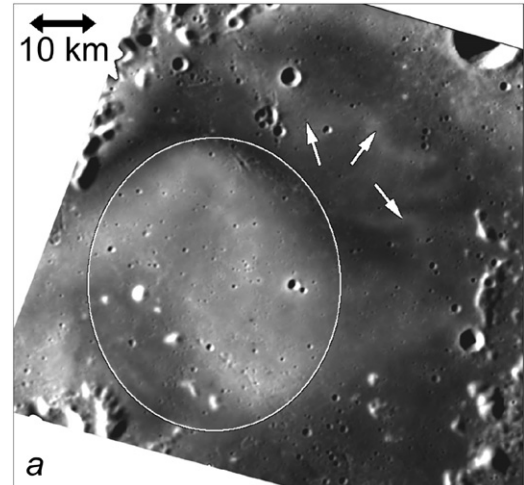


**Fig. 10.** Swirl in Mare Ingenii: (a) reflectance image at 107° phase (AMIE frame 2871/16); (b) parameter of phase steepness  $\eta$  obtained from  $f(83^\circ)/f(107^\circ)$  phase ratio; (c) optical maturity parameter OMAT by Clementine data. Arrows point to small swirl features. Outlined is a high albedo swirl detail 35 km across indistinguishable on the  $\eta$  map.

farside swirls. We combined a pair of images 142/40 and 2871/16 obtained at large phase angles,  $\alpha = 83^\circ$  and  $107^\circ$ , respectively. The area imaged covers a portion of crater Thomson M in Mare Ingenii and shows a large oval-shaped swirl (35 km in size, outlined) as well as several small diffuse albedo details. Fig. 10a is a portion of  $107^\circ$  phase-angle frame; arrows show small swirl details al-

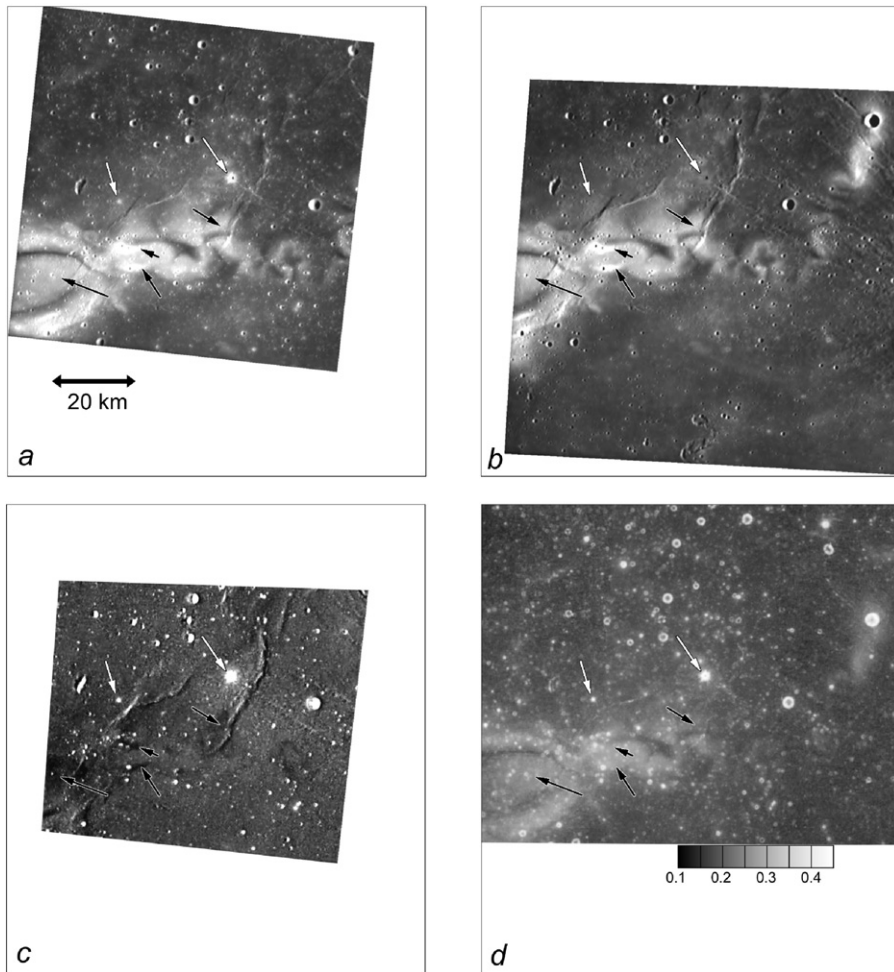


**Fig. 11.** Reiner Gamma swirl: (a) reflectance image at 56° phase (AMIE frame 1781/41); (b) reflectance image at 98° phase (AMIE frame 1918/6); (c) parameter of phase steepness  $\eta$  obtained from  $f(56^\circ)/f(98^\circ)$  phase ratio; (d) optical maturity parameter OMAT by Clementine data. White arrows point to positive anomalies, black arrows point to the most prominent low- $\eta$  details.

ternated with dark mare material. Here we face the problem of opposite illumination directions for the images constituting a pair. This effect exaggerates surface topography manifestation, even if tilts are very gentle; however, for flat mare surfaces mapping of  $\eta$  is still reliable. The outlined swirl feature does not show up in the  $\eta$  parameter map; only small swirl details pointed by arrows can be distinguished. Despite the poor mapping conditions, we are sure that the strong variations of  $\eta$  observed for Mare Marginis in association with swirl features are absent in this scene.

### 3.3.3. Reiner gamma swirl

To calculate phase-angle ratio for this area we took two images of a scene east from the Rainer Gamma Swirl (RGS) core, 1781/41 and 1918/6 (see Table 1 for image parameters). The 56° and 98° phase-angle reflectance images are presented in Figs. 11a and 11b. Visual comparison of lower- and higher-phase images reveals two craters with bright halos perfectly seen in the smaller-phase-angle frame and almost vanished in the larger-phase-angle image (shown with white arrows in Fig. 11). The  $\eta$  map presented in Fig. 11c shows these craters as strong positive photometric anomalies. These features are analogous to two features marked with white arrows in Fig. 3. The most prominent negative photometric anomalies associated with bright swirl details are shown with black arrows in Fig. 11.

We made a phase ratio  $f(30^\circ)/f(61^\circ)$  image for the RGS core and mare area to the north of it using 2243/7 and a mosaic of 2110/13 and 2110/12 frames (see image parameters in Table 1). This

scene (Fig. 12) partly overlaps with the photometric anomaly map made by Kreslavsky and Shkuratov (2003) from Clementine data. The distribution of  $\eta$  for the overlap area is remarkably similar. White arrow (Fig. 12) points to one more compact strong crater-related positive photometric anomaly, the only object of this kind encountered by Kreslavsky and Shkuratov (2003).

### 3.3.4. Crater Louise

This scene features small 0.8 km-size crater Louise (Fig. 13) located in western portion of Mare Imbrium between Diophantus (seen in the lower edge of the scene) and Delisle (in the upper part of the scene). We applied the phase ratio method to this scene using 518/9 and 635/14 images (see Table 1) obtained at  $\alpha = 18^\circ$  and  $35^\circ$ , respectively. Rough proximal ejecta of Delisle and Diophantus come out at the phase steepness image (Fig. 13b) as illuminated topography due to surface tilts, however, for the flat surfaces containing Louise rays the method is reliable. We also verified that the surface here is flat with the high resolution Apollo 15 metric frame AS15-M-2075 (<http://apollo.sese.asu.edu/webmap-bin/apollo.pl>) (Fig. 13c). The visual inspection shows that the local topography is complicated by a number of secondary craters of Delisle and also by Rima Diophantus, nevertheless, there is no large-scale relief associated with the distal Louise ejecta.

### 3.3.5. Part of Olbers A ray

Crater Olbers A ( $77.6^\circ$  W,  $8^\circ$  N) has an extensive ray system. We analyzed a small portion of it near an intersection of two ma-

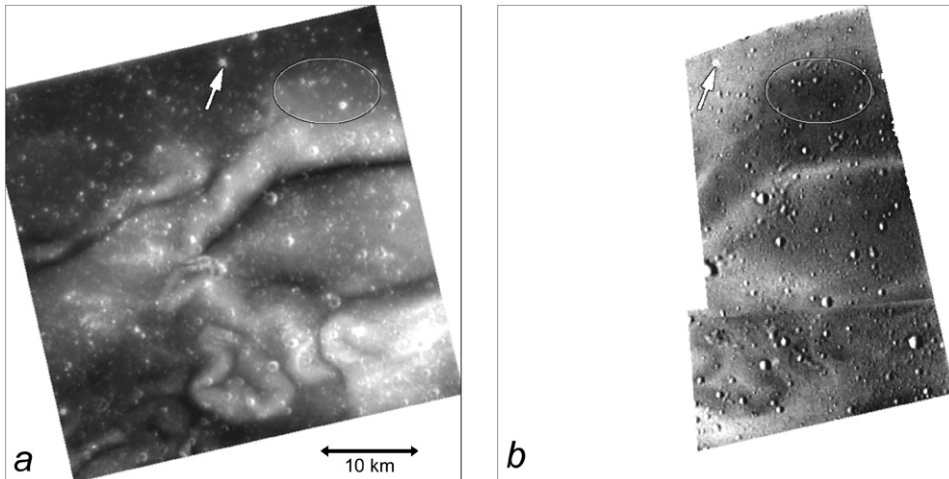


**Fig. 12.** Reiner Gamma swirl core: (a) reflectance image at  $30^\circ$  phase (AMIE frame 2243/7); (b) parameter of phase steepness  $\eta$  obtained from  $f(30^\circ)/f(61^\circ)$  phase ratio. Brighter shades on the  $\eta$  map denote greater steepness. Phase steepness map is mosaicked from two parts. White arrow points to a positive anomaly associated with bright small mare crater, outlined is part of the swirl with intermediate albedo and low  $\eta$  values.

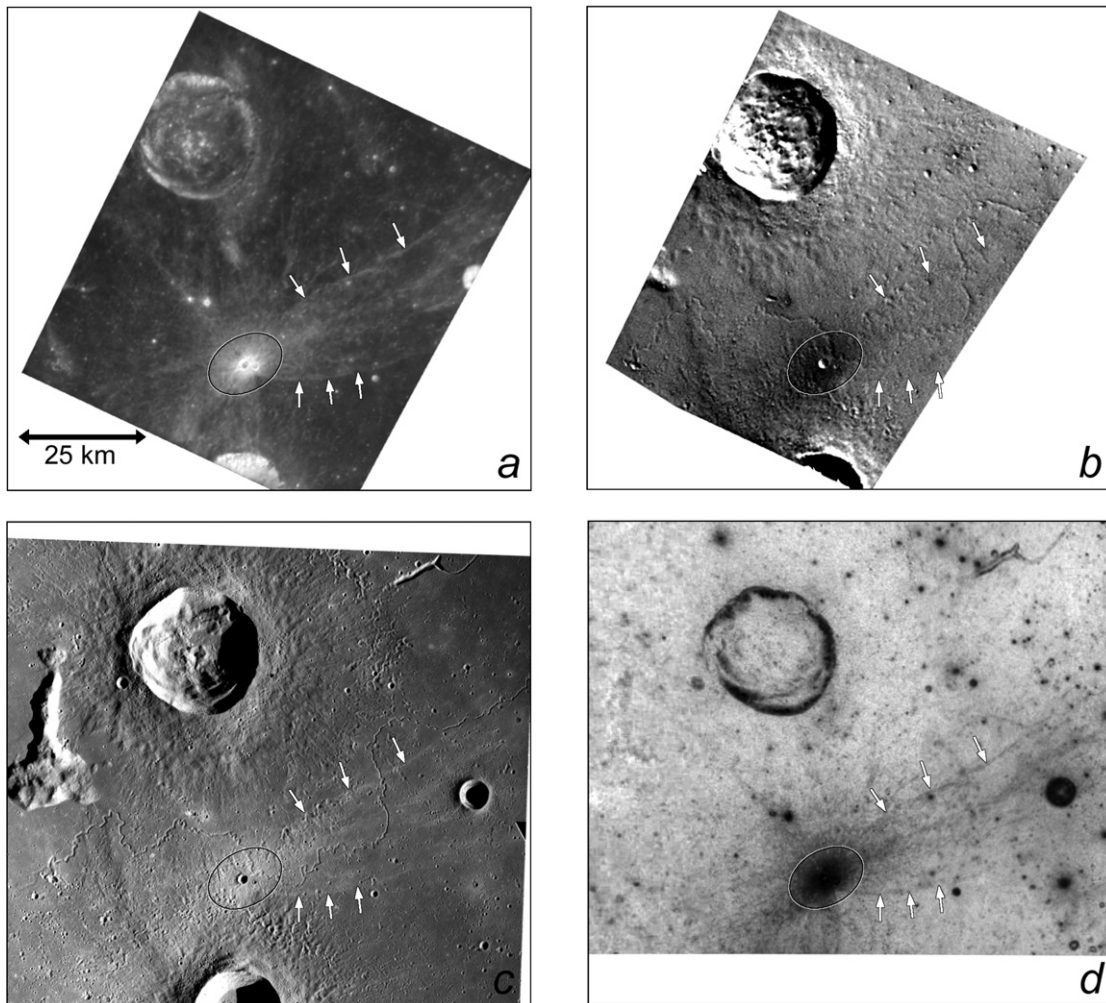


**Fig. 13.** Ray system of crater Louise: (a) reflectance image at  $18^\circ$  phase (AMIE frame 635/14); (b) parameter of phase steepness  $\eta$  obtained from  $f(18^\circ)/f(35^\circ)$  phase ratio; (c) part of high resolution Apollo-15 image AS15-M-2075; (d) Clementine color ratio  $C_{IR}(950/750 \text{ nm})$ ; brighter shades denote greater  $C_{IR}$ , which generally corresponds to more mature regolith. Outlined is the low- $\eta$  central part Louise ejecta. White arrows point to Louise rays indistinguishable on the  $\eta$  map. The largest crater in the scene is 26 km-sized Delisle.

jor ray elements ( $68^\circ$  W,  $16.5^\circ$  N) about 385 km northeast from Olbers A crater (Fig. 14a). We used AMIE images 40/64 and 114/76 to make the phase ratio  $f(43^\circ)/f(71^\circ)$  and the image of the phase

function steepness parameter (Fig. 14b). The  $\eta$  parameter image reveals the mare wrinkle ridge extending in south-north direction. In the flat part of the scene there are areas of low  $\eta$  associated with

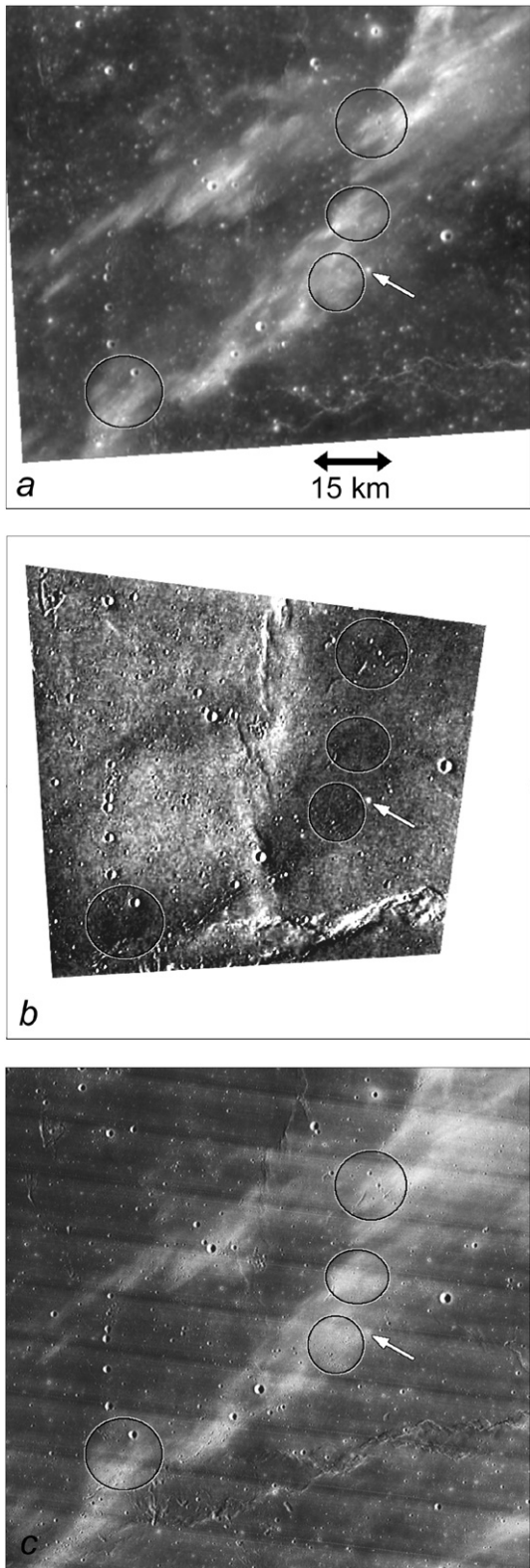


**Fig. 14.** Part of Olbers A ray: (a) reflectance image at 43° phase (AMIE frame 40/64); (b) parameter of phase steepness  $\eta$  obtained from  $f(43^\circ)/f(71^\circ)$  phase ratio; (c) part of high resolution LO IV image 4169\_H2. Outlined are the lowest- $\eta$  parts of Olbers A ray. White arrow points to a small mare crater appearing as a positive photometric anomaly.

the rays; we outlined the most prominent parts. The high resolution LO IV image 4169\_H2 does not show any apparent topography associated with the ray pattern (Fig. 14c). This scene gives one more example of a compact strong positive photometric anomaly

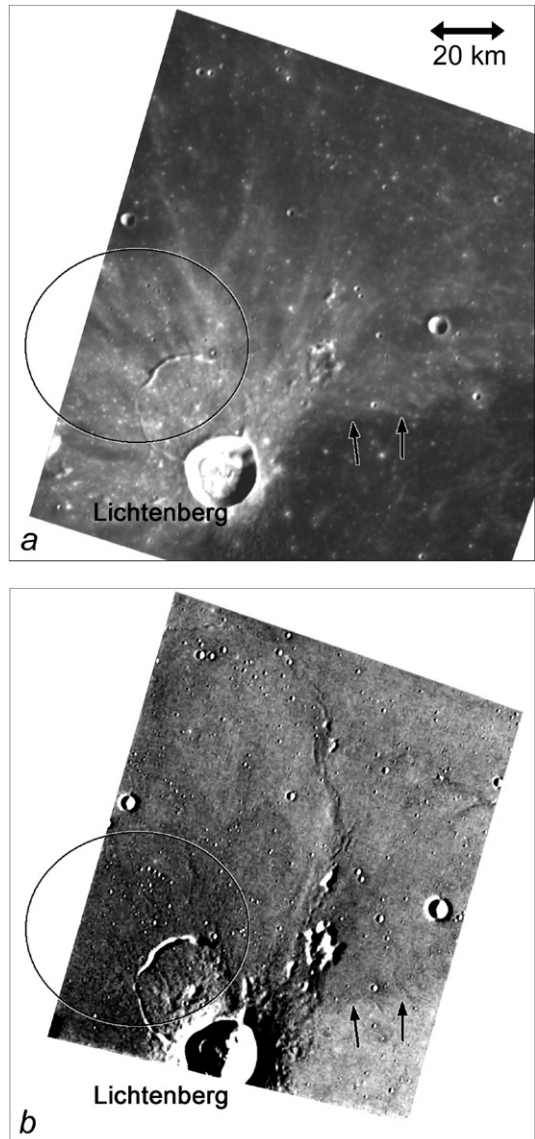


**Fig. 15.** Lichtenberg ray system: (a) reflectance image at 73° phase (AMIE frame 114/94); (b) parameter of phase steepness  $\eta$  obtained from  $f(44^\circ)/f(73^\circ)$  phase ratio. Outlined areas are the lowest- $\eta$  parts of Lichtenberg ejecta blanket. Arrows point to the albedo boundary easily distinguishable on  $\eta$  distribution.

(arrow) associated with a compact bright halo of a small impact crater, as is seen in the LO image (Fig. 14c).

### 3.3.6. Lichtenberg ray system

Crater Lichtenberg in northwestern part of Oceanus Procellarum has high albedo ejecta superimposed on dark mare basalts (Fig. 15a). We took frames 40/85 and 114/94 (see Table 1 rows for Lichtenberg) and mapped the phase steepness from  $f(44^\circ)/f(73^\circ)$  phase ratio (Fig. 15b).

We made a phase function steepness map from the  $f(38^\circ)/(74^\circ)$  phase ratio using another pair of AMIE frames in the same scene, 530/9 and 2110/9 (Fig. 16a). These images have higher resolution than those used for Fig. 15. This phase function steepness map reveals three small high- $\eta$  spots (white arrows, Fig. 16) that directly correspond to small craters (400–500 m size) seen in the high resolution LO IV image 4170\_H1 (Fig. 16b). This image pair also gives another example of a low- $\eta$  halo around two small bright craters (black arrow); this halo is ~2 times larger than the craters; it does not distinctively show up in the albedo image. This

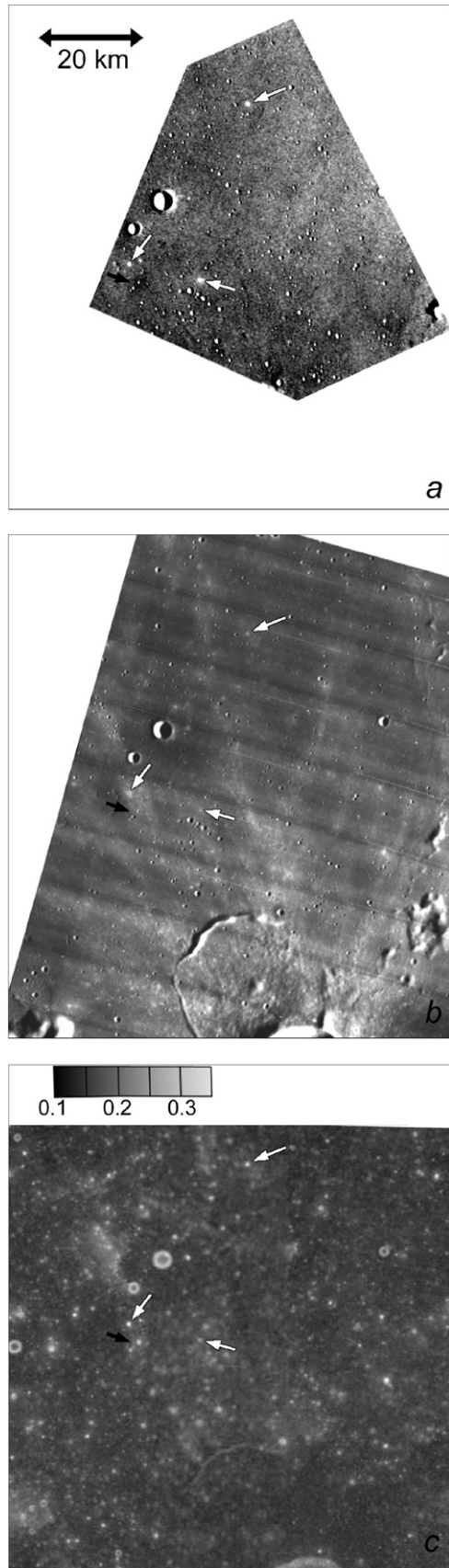


**Fig. 16.** Enlarged part of Lichtenberg rays: (a) parameter of phase steepness  $\eta$  obtained from  $f(38^\circ)/f(74^\circ)$  phase ratio; (b) part of high resolution LO IV image 4170\_H1; (c) optical maturity parameter OMAT by Clementine data. White arrows point to small mare craters appearing as positive photometric anomalies. Black arrow points to the low- $\eta$  halo around two small bright craters.

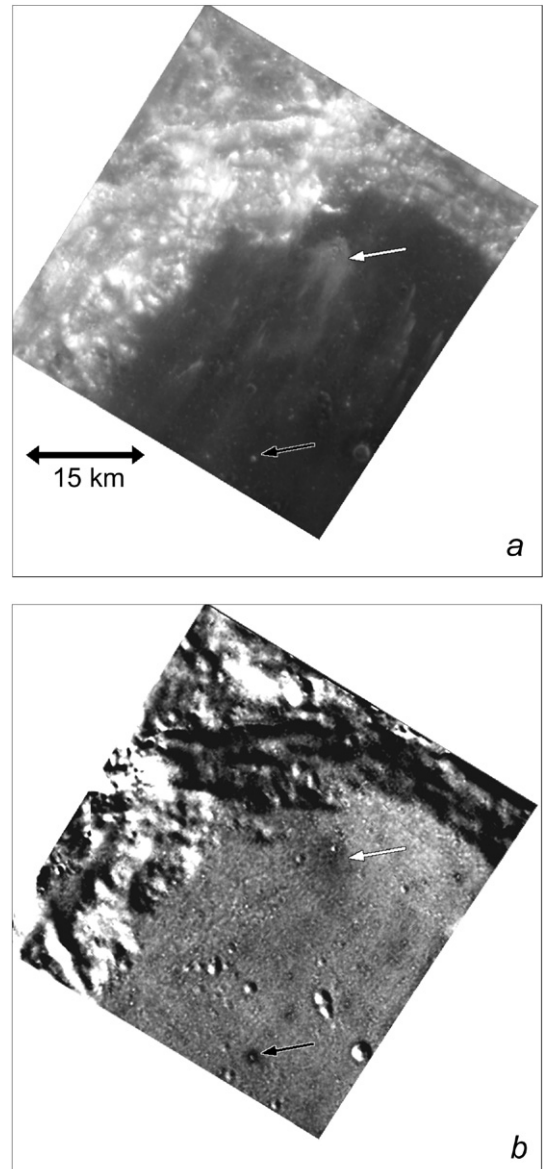


**Fig. 17.** Lomonosov floor: (a) reflectance image at  $15^\circ$  phase (AMIE frame 2319/10); (b) parameter of phase steepness  $\eta$  obtained from  $f(15^\circ)/f(40^\circ)$  phase ratio. White arrow points to a secondary crater with ejecta; black arrow denote a small crater with low- $\eta$  halo.

feature looks similar to the features marked with black arrows in Fig. 3.

### 3.3.7. Lomonosov floor

A large 92 km farside crater Lomonosov ( $102.8^\circ$  E,  $35.9^\circ$  N) was filled by lava after the impact, thus exhibiting a flat floor. The crater contains ejecta deposits and secondary impact craters from crater Giordano Bruno located 280 km approximately to northeast. Fig. 17a present a view of Lomonosov obtained at  $15^\circ$  phase angle. Here we faced with almost two times difference in spatial resolution of SMART-1 AMIE images (for  $15^\circ$  and  $40^\circ$  phase) used. We reduced the spatial resolution to the worst one with the Gaussian smoothing. The  $f(15^\circ)/f(40^\circ)$  phase ratio (Fig. 17b) reveals no distinctive details on the floor except the low- $\eta$  feature (white arrow) associated with the central part of ejecta blanket centered around a small crater, perhaps, a Giordano Bruno secondary. Another detail showing up in the phase ratio is also low- $\eta$  halo around a small crater shown with black arrow. This halo is not

associated with any prominent albedo increase close to the crater. We believe that the low- $\eta$  halo was produced by the same process as for small craters in the Gruithuisen domes scene (Fig. 3, black arrows).

### 3.3.8. Southern part of Mare Serenitatis

One more scene in our survey is located in the southern portion of Mare Serenitatis (Fig. 18a). The dark albedo feature at the bottom of the image is the Serenitatis/Tranquilitatis boundary. We mapped the phase function steepness with the  $f(43^\circ)/f(63^\circ)$  phase ratio (Fig. 18b). The AMIE images 2214/11 and 2082/1,2,3 were used (see Table 1). To enhance the quality of the phase ratio, we averaged three larger-phase-angle images 2082/1, 2082/2, and 2082/3 acquired under very similar illumination/observation conditions. A set of wrinkle ridges is seen in the northern part of the  $\eta$  map, including a gentle ridge neither apparent in the source images nor seen in a high-resolution Apollo-15 image (Fig. 18c). Unlike the wrinkle ridges and craters, an elongated bright feature in the southern part of the  $\eta$  map (Fig. 18b) does not look like illuminated topography, but we cannot exclude the possibility that it is related to a topographic scarp not apparent in Figs. 18a and 18c. White arrow points to one more example of a strong compact positive photometric anomaly associated with a small crater.

### 3.3.9. Western Procellarum near Briggs

Crater Briggs (37 km) in Western Procellarum was formed in the Late Imbrian period (Wilhelms, 1987). The SMART-1 AMIE image 40/75 presents an area in western Procellarum in the vicinity of crater Briggs (Fig. 19a). We used this image together with the 114/86 (see Table 1 for image details) to make a  $f(43^\circ)/f(72^\circ)$  phase ratio image and map the phase function steepness (Fig. 19b). The  $\eta$  map mainly reveals the topography features (wrinkle ridges) in the scene. Analysis of the low-Sun high-resolution LO IV image 4169\_H3 (Fig. 19c) does not give evidence for any detectable topography associated with the boundary between mare units pointed by arrows. Both the NE-SE-trending ray in the SE corner of the image and the albedo boundary shown with arrows do not have any expression in the  $\eta$  map.

### 3.3.10. North–West part of Mare Imbrium

The last scene in our survey is located in the northwestern part of Mare Imbrium just south to Sinus Iridum. We used two SMART-1 AMIE images, 105/98 and 516/9, for the photometric analysis of this region centered at 28.8° E, 39° N (Table 1). Fig. 20a shows the reflectance image obtained at 43° phase angle. The parameter of phase function steepness (Fig. 20b) obtained from the  $f(43^\circ)/f(73^\circ)$  phase ratio beautifully reveals a set of wrinkle ridges. The albedo boundary, marked with arrows has no expression on the  $\eta$  map.

## 4. Interpretation

### 4.1. Lunar swirls as seen by SMART-1

The origin of lunar swirls, diffuse bright albedo features with no signs of topography, is one of most intriguing problems in lunar science; it has been extensively debated in scientific literature (see, e.g., Pinet et al., 2000; Starukhina and Shkuratov, 2004, and references therein). Understanding their origin would be a clue to the important phase of lunar surface evolution. Both Earth-based and orbital studies reveal unusual photometric properties of lunar swirls. The unusual photometric behavior of swirls at large phase angles was noted by Schultz and Srnka (1980) from qualitative analysis of Apollo and Lunar Orbiter photographs. Kreslavsky and Shkuratov (2003) described the Reiner–Gamma Swirl (RGS) as

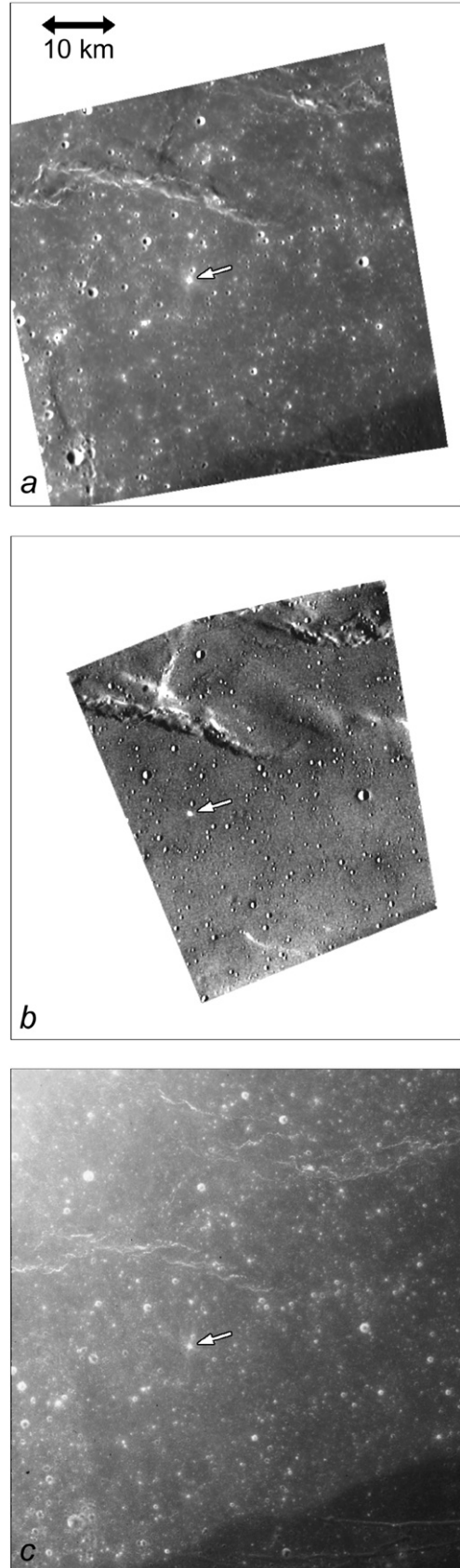


**Fig. 18.** Southern part of Mare Serenitatis: (a) reflectance image at 63° phase (AMIE frame 2082/3); (b) parameter of phase steepness  $\eta$  obtained from  $f(43^\circ)/f(63^\circ)$  phase ratio; (c) part of high resolution Apollo image AS15-M-1803. Arrow points to a small crater with a positive photometric anomaly. Dark albedo feature at the bottom is Serenitatis/Tranquilitatis border.

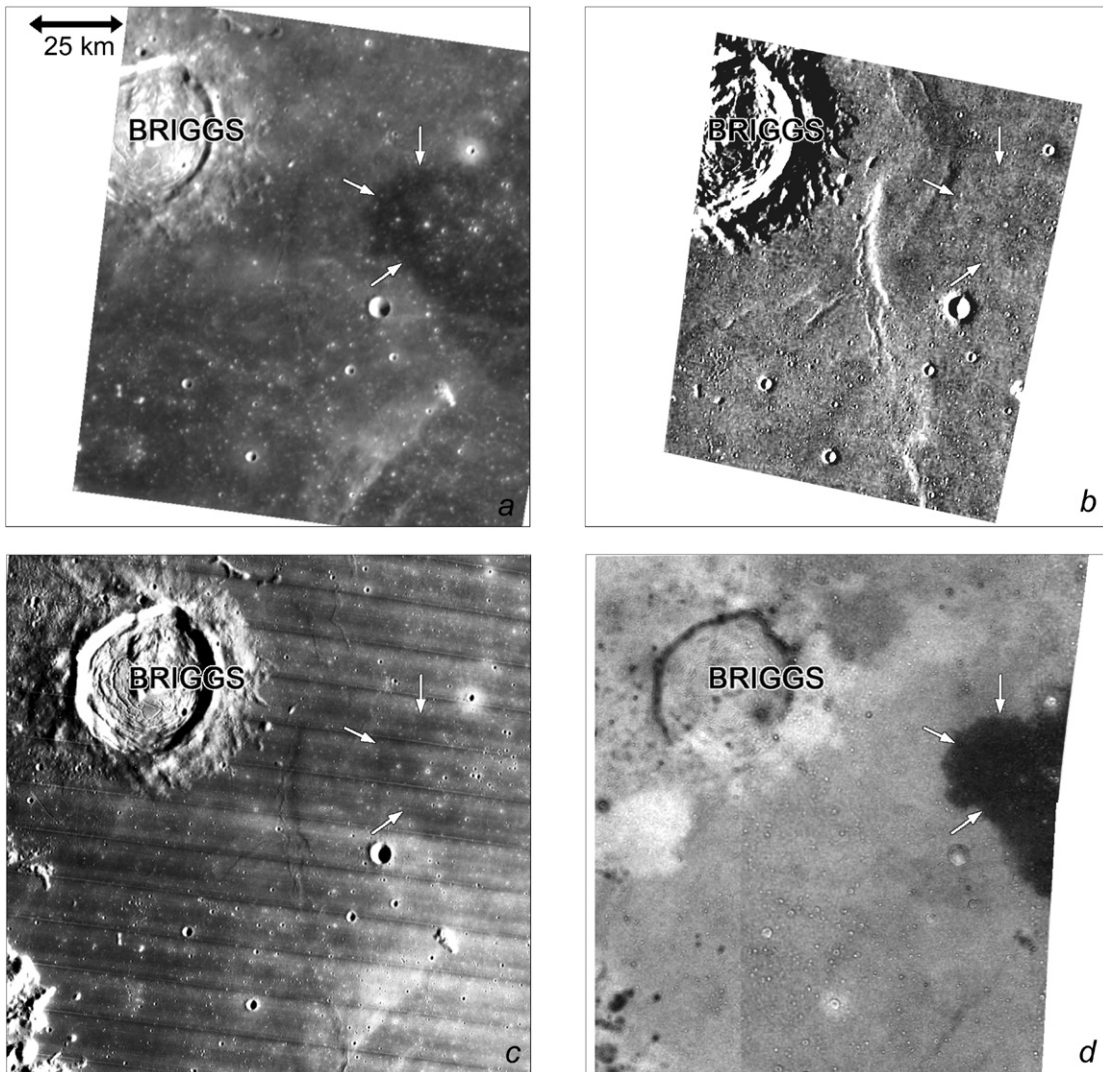


**Fig. 19.** Western Procellarum near Briggs: (a) reflectance image at 43° phase (AMIE frame 40/75); (b) parameter of phase steepness  $\eta$  obtained from  $f(43^\circ)/f(72^\circ)$  phase ratio; (c) part of high resolution LO IV image 4169\_H3; (d) Clementine color ratio  $C_{\text{VIS}}(750/415 \text{ nm})$ ; brighter shades denote greater  $C_{\text{VIS}}$ . White arrows point to albedo and color feature, which is invisible on the  $\eta$  map.

a negative photometric anomaly, with variations of the millimeter-scale regolith structure within the RGS. The SMART-1 spacecraft has imaged several lunar swirls from different orbits, thus providing data for the phase ratio mapping.

For the RGS, the SMART-1 data (Figs. 11 and 12) confirm that the bright surface of the swirl is associated with generally low values of  $\eta$ . However, within the negative anomaly spots, the absolute values of  $\eta$  do not correlate with albedo. The most evident example is marked in Fig. 12: the outlined part of the scene is much darker than adjacent terrain to the south, but shows the same values of the phase curve steepness parameter. A number of bright details seen in the image (Fig. 11a) are almost indistinguishable in the phase function steepness map (Fig. 11b). More examples of this kind have been presented by Kreslavsky and Shkuratov (2003). This absence of an inverse correlation between albedo and  $\eta$  indicates that the low values of  $\eta$  for the RGS cannot be explained solely by the mechanism of shadow lightening; the variations of  $\eta$  certainly reflect some significant variations of the surface structure. Knowing that moderately large to large (30–100°) phase angles are involved, these variations of structure are probably variations of the roughness at a millimeter scale and, possibly, up to a decimeter scale.

In the map of the optical maturity parameter (OMAT) (Fig. 11d), the RGS shows up as an area of moderately immature regolith (moderately elevated OMAT values) with an average OMAT values of 0.27–0.28. Visual comparison of OMAT and  $\eta$  distributions reveal that there is no tight correlation between them. For example, the distinctive low- $\eta$  details marked with black arrows (Fig. 11c) do not have the corresponding local OMAT maxima (Fig. 11d). This again points that the RGS has variations of the surface structure at scales larger than the scales primarily responsible for the optical maturity (nanometers to microns). Note that variations of roughness in the regolith were also suggested for RGS by Pinet et al. (2000).

The swirl in Mare Marginis covers a huge area, almost the whole Mare Marginis region and highlands to north of it and north of crater Goddard. This swirl actually looks like a number of bright albedo features up to tens of kilometers across; these diffuse features are best seen when superimposed on a dark flat mare surface. The scene in Fig. 9a contains a few examples of such features mostly seen in the right part of the image. Similarly to the RGS, our map of  $\eta$  (Fig. 9b) shows diffuse swirl details as distinctive features of low phase function steepness. Arrows point to the most pronounced parts of such features. Similarly to the RGS, the

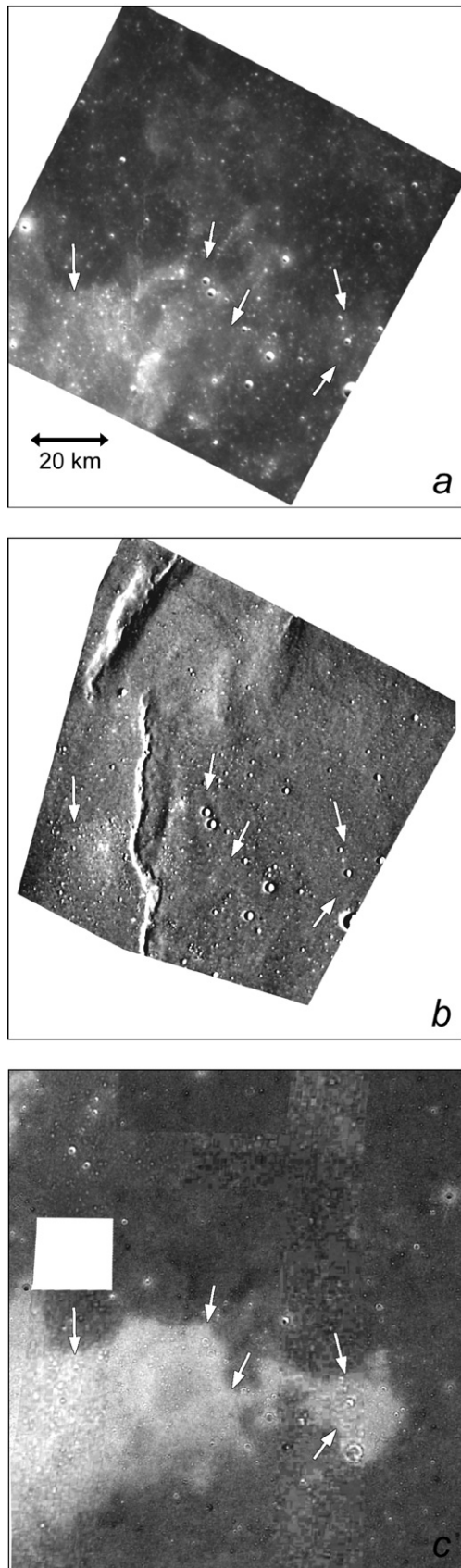


**Fig. 20.** North-West part of Mare Imbrium: (a) reflectance image at 43° phase (AMIE frame 516/9); (b) parameter of phase steepness  $\eta$  obtained from  $f(43^\circ)/f(73^\circ)$  phase ratio; (c) Clementine color ratio  $C_{\text{VIS}}(750/415 \text{ nm})$ ; brighter shades denote greater  $C_{\text{VIS}}$ . Arrows point to albedo and color feature which disappears on the  $\eta$  map.

swirls have elevated values of OMAT (Fig. 9c). Unlike the case of the RGS, there is a rather tight inverse correlation both between  $\eta$  and albedo and between  $\eta$  and OMAT. However, the sample is too small to conclude that the observations imply a significant difference between the nature of the RGS and the nature of the swirl in Mare Marginis.

The scene in Mare Ingenii (Fig. 10a) covers a portion of crater Thomson M and shows a large oval-shaped swirl (35 km in size, outlined) as well as several smaller weaker diffuse albedo details. OMAT (Fig. 10c) correlates well with albedo for swirl features. We found that the  $\eta$  parameter map calculated from the phase ratio  $f(83^\circ)/f(107^\circ)$  (Fig. 10b) reveals no inverse correlation between the phase function steepness and albedo for the bright pattern formed by swirl in Mare Ingenii (Fig. 10b). According to our  $\eta$  map, only small swirl features pointed by white arrows show weak resemblance to inverted albedo. These features are also barely distinguishable on the optical maturity map (Fig. 10c).

It would be reasonable to anticipate that the nature of the swirl surface is similar for all swirls, and the observed difference between swirls in Mare Ingenii on one hand and swirls in Mare Marginis and the RGS on the other hand is due to the difference in the phase angles used for the  $\eta$  mapping rather than in the nature of the surface. As has been discussed in Section 2.6, the dependence of brightness on phase angle for large  $\alpha$  is mostly affected by the meso- and macro-topography. Thus, Fig. 10 suggests that the contribution of these scales to the peculiar swirl properties is weak or absent, hence, the specific and varying regolith structure of swirls is limited to smaller scales. We would like to note that reliable confirmation of the variations of regolith structure in mm-cm scale requires photometric studies of Mare Ingenii region at smaller phase angles.

#### 4.2. Crater rays

Three classes of lunar crater rays are usually considered (e.g., Hawke et al., 2004): (a) mature “compositional” rays (due to contrast in albedo between ray material containing non-mare material and the adjacent dark mare surfaces), (b) “immaturity” rays (visible because of fresh bright material contrasting with mature neighborhood), (c) a combination of (a) and (b). Craters and their ray systems may contain both local (chemically identical) and delivered from distant sources (chemically different) material of different maturity with variations of surface roughness that is formed with debris, boulders, blocks, and secondary crater clusters. Our survey of photometric properties contains a few examples of crater rays of different origin.

Fig. 14 shows a small part of the extensive ray system of Olbers A near an intersection of two major ray elements. Analysis by Hawke et al. (2004) has shown that the most of Olbers A ray segments are not distinct in the optical maturity map, thus the dominant factor responsible for the high albedo of these segments is the presence of highland-composition ejecta from Olbers A. Bright ray segments (Figs. 14a and 14c) correspond to decreased values of the phase function steepness  $\eta$ . We outlined the most prominent low-steepness spots (ellipses); visual comparison shows a tight inverse correlation with albedo features. The source images are taken at a large phase angles ( $43\text{--}71^\circ$ ); therefore, one can expect that both shadow hiding and mesorelief govern the steepness of the phase function. Weakening of shadow hiding due to shadow lightening in brighter materials is apparently responsible for the observed inverse correlation. If the roughness of the rays were significantly higher in comparison to surroundings, the phase function would be steeper, which is not observed. The absence of a significant roughness increase is consistent with complete optical maturity: for these old ray system the mesoscale surface structure evolved toward the equilibrium.

Crater Lichtenberg (Figs. 15 and 16) in northwestern part of Oceanus Procellarum has high albedo ejecta superimposed on dark mare basalts (Fig. 15a). Situation here is very similar to what we observed for the Olbers A ray above. According to Hawke et al. (2004) the brightness of the Lichtenberg rays is produced only by compositional differences between the mature highlands-rich ray material and the adjacent mature mare surfaces. So the Lichtenberg ejecta are also fully mature (see OMAT map in Fig. 16c), and the phase function steepness map also shows a general weak decrease of  $\eta$  in the ejecta area.

Situation is different for crater Louise (Fig. 13). Despite the rather small size of this crater, its ejecta extend more than 50 km to the northeast and 20–25 km in other directions. The northeastern lobe (>50 km) of Louise ejecta (arrows) is not distinguishable on the image of the phase function steepness (Fig. 13b) and only a 10 × 15 km ellipsoidal ejecta core (outlined) shows itself as a low- $\eta$  feature. The phase angles of the source images are rather low ( $18^\circ$  and  $35^\circ$ ). At these phase angles the shadow hiding effect should influence the phase function. For brighter rays, shadow lightening should decrease the phase function steepness in comparison to surroundings. The absence of such a decrease indicates that shadow lightening is compensated by some other effect, perhaps, by increased roughness at <1 mm scale, the scale that most effective for given phase angles.

It is interesting to compare these results with the regolith maturity. The Clementine color ratio  $C_{IR}(950/750 \text{ nm})$  presented in Fig. 13d shows low values of  $C_{IR}$  for the outlined proximal ejecta zone as well as for distal Louise ejecta. This indicates that the 1-μm absorption band in reflectance spectrum is rather deep and, hence, the ejecta regolith is immature (e.g., Lucey et al., 2000b; Pieters et al., 2006). It seems to be natural that the immature regolith is accompanied with increased roughness, as it follows from the photometric properties.

#### 4.3. Anomalies related to small craters

Our data set gives a number of examples of photometric anomalies associated with small (tens of meters to a kilometer) impact craters. These anomalies are of two kinds, positive and negative. Negative anomalies (marked with black arrows in the figures) were found in the following scenes: Gruithuisen domes (3 features) (Fig. 3), crater Lavoisier (2) (Fig. 7), Lichtenberg (1) (Fig. 16), and Lomonosov floor (1) (Fig. 17), totally 7 features. Kreslavsky and Shkuratov (2003) have found 3 more examples of this kind. The negative crater-related anomalies look like darkened diffuse halos around central craters in the maps of the phase function steepness. Images clearly show that these anomalous halos are larger than the bright high-albedo halos of the craters (if such bright halos are present), thus the anomalous photometric behavior here is not immediately caused by the albedo variations and reflects changes in the surface structure.

Positive anomalies (marked with white arrows in the figures) were found in the following scenes: Gruithuisen domes (2 features) (Fig. 3), Reiner Gamma (3) (Figs. 11 and 12), Olbers A ray system (1) (Fig. 14), Lichtenberg (3) (Fig. 16), and Mare Serenitatis (1) (Fig. 18), totally 10 features, including one found earlier by Kreslavsky and Shkuratov (2003). The positive anomalies are very strong, they occupy sharply shaped compact areas just around the central craters and usually coincide with bright proximal ejecta; in one case (Mare Serenitatis scene, cf. Figs. 18b and 18c) short bright rays extend beyond the limits of the photometric anomaly.

We compared our  $\eta$  map with the distribution of the optical maturity parameter OMAT calculated by the method of Lucey et al. (2000b) (cf. Figs. 3b and 3d, 16a and 16c). Visual inspection shows that all small photometric anomalies (both positive and negative) are linked to high-OMAT details (i.e. immature regolith), although

the negative anomalous halos are larger than corresponding OMAT features (cf. Figs. 3b and 3d).

We interpret the negative crater-related photometric anomalies following Kreslavsky and Shkuratov (2003). The equilibrium state of the uppermost regolith surface is known to be produced by the space weathering processes, most importantly, the micrometeorite bombardment, at geologically short timescale. As a result, the uppermost millimeter-scale regolith layer has a porous open-work ("fairy castle") structure. Meteoritic impact events destroy this porous structure in some vicinity of the impact, make surface smoother and hence make the phase function less steep. Two possible mechanisms of this regolith structure modification can be envisioned. The openwork structure could collapse due to a ground shock/seismic wave produced by the forming impact, which shakes the regolith. Alternatively, this structure could be disrupted by a sparse shower of fine-grain distal ejecta that are dense enough to destroy the porous structure, but having particles too small to overturn the regolith and expose immature soil. The proximal ejecta are bright and immature due to the deposition of freshly excavated material and overturning of the regolith. With time, the equilibrium openwork structure of the soil is reestablished and immature soil matures. The time scale of the structure equilibration is perhaps shorter than the time scale of spectral maturation, which explains the presence of immature craters without negative photometric anomalies. Both time scales are short in comparison to the geological age of the mare surfaces, which explains the total small number of the anomalous craters.

We interpret the positive anomaly for craters as an increase of mesoscale roughness in the proximal ejecta zone, making the phase function steeper. This roughness can be due to the presence of an anomalously large number of boulders, blocks, rock fragments within the proximal ejecta of the craters, which produces extremely rough (at scales from centimeters to meters) surface. Correlation with high OMAT index is naturally explained. First, the impact simultaneously excavates blocks and immature regolith, in this case the immature overturned soil can extend beyond the rocky area (as in the Mare Serenitatis scene, Fig. 18). Then, with geological time, distal parts of the ejecta mature, while in the proximal area, in the presence of abundant, densely spaced blocks, continuous wasting of newly forming soil from steep facets of the blocks keeps the regolith immature. Thus, for relatively older anomalous craters, the spectrally immature area would coincide with the photometric anomaly, exactly what we observe in a number of examples.

It is not clear, why some craters have anomalously dense population of blocks in the proximal ejecta. One possibility is that some unusual effects can occur during the impact, if the excavation depth is close to the local thickness of mechanically stronger mare basalts that overlay mechanically weaker megaregolith. Another possibility is some peculiar property of the projectile (e.g., velocity).

#### 4.4. Compositional variations

In this section we discuss relation between photometric properties and composition of lunar mare materials. A weak small-scale composition-related photometric anomaly has been found with Clementine data by Kreslavsky and Shkuratov (2003): in one site the decrease of the red/blue color ratio  $C_{VIS}$  (750/415 nm) accompanies a weak negative photometric anomaly. In a recent telescopic survey with the phase ratio  $23^\circ/44^\circ$  (Gerasimenko et al., 2008) three large areas in Mare Nubium and southern Oceanus Procellarum have been identified as positive photometric anomalies accompanied by an increase of the  $C_{VIS}$  parameter; note that this is an effect of the same signature. Below we consider a few examples from SMART-1 image data set.

There is an albedo boundary in the lower right part of the Lichtenberg scene (arrows in Fig. 15a). This feature corresponds to distinct chemical differences in terms of iron and titanium content (Lucey et al., 2000a; Blewett et al., 1997). The boundary is very well seen in the  $\eta$  map (Fig. 15b): the brighter side of the boundary has less steep phase function, which would be expected to result from shadow lightening.

Similar boundaries between brighter and darker mare materials are seen in the Briggs and NW Imbrium scenes (arrows in Figs. 19 and 20). The phase angles of the source images for these scenes are almost the same as for Lichtenberg. However, in these two cases, the boundaries are not distinguishable in the phase ratio images (Figs. 19b and 20b). This means that the difference in the photometric behavior caused by shadow lightening should be compensated by some other mechanism. There is no noticeable change of OMAT parameter associated with those boundaries. Mapping the color ratio  $C_{\text{VIS}}$  with Clementine data shows a distinct color contrast across the boundaries (Figs. 19d, 20c): the brighter units are much redder, indicating a significant difference in composition. We suggest that the brighter redder units have a little more porous uppermost regolith layer, which compensates the effect of the higher albedo on the phase function; the difference in porosity is controlled by the difference in composition and hence in mineralogy and mechanical properties of the soil particles.

## 5. Conclusion

Our study of SMART-1 AMIE data reveals photometric anomalies, from subkilometer to tens of kilometer sizes. The presented examples demonstrate the use of lunar orbital multiangular photometry to characterize the regolith microstructure; they illustrate both the usefulness of spot-pointing imaging observations and the scientific value of the AMIE data in documenting geological and surface processes associated with floor-fractured craters, pyroclastic deposits, ray systems of different origin, and swirls.

Three lunar swirls studied in the paper revealed both the similarity of regolith mesoscale roughness with surrounding terrains (Mare Marginis and Mare Ingenii swirls) and details with unique photometric properties related to peculiarities of the millimeter-scale regolith structure (Reiner Gamma swirl).

A number of impact craters of subkilometer sizes were identified with the method of phase ratios as positive photometric anomalies interpreted as an increase of mesoscale roughness in the proximal crater ejecta zones making the phase function steeper. This roughness can be due to the presence of boulders and blocks produced by impact events. It is interesting that only a few craters among a large number of craters of the same size possess this property.

The photometric study of extended ray systems of the craters Louise, Lichtenberg, and Olbers A revealed differences in the photometric properties of proximal and distant ejecta blankets and also confirmed the different nature of those ray systems.

We tested the method of phase ratios for two mare regions in Mare Imbrium and Western Procellarum characterized by large scale variations of color ratios in the Clementine UVVIS spectral range. Unusual photometric properties we found for those regions may be associated with the presence of rougher regolith surface for redder mare soils. Those differences in regolith roughness would be related with chemical composition of basaltic lava flows of different ages.

The detailed study of lunar photometric function requires paving the domain of photometric angles with a rather dense mesh. The common way to perform such measurements is to apply the spot-pointing technique from different lunar polar orbits of a spacecraft. Unfortunately, due to the hardware and orbital constraints, the spot-pointing possibilities are usually limited to a

few sites, like in the Clementine and SMART-1 missions. Another possibility to increase the amount of data suitable for carrying photometric analyses is the combined use of Clementine UVVIS and AMIE datasets (Shkuratov et al., 2003). Recent data from the JAXA Kaguya mission obtained with the Terrain Camera and Multi-band Imager will also be extremely useful to complement the data available with an improved spatial resolution on the lunar surface about 10–60 m. New images from CCD cameras onboard Chinese Chang'e, Indian Chandrayaan-1 and NASA's LRO also would help to produce combined brightness phase ratios and analyze them in terms of regolith physical properties. Cross-calibration of diverse multi-national instruments (Pieters et al., 2008) will allow joining these datasets and mapping photometrical properties with unprecedented spatial resolution.

## Acknowledgments

We are greatly thankful to Deborah Domingue and an anonymous reviewer for insightful reviews. Their comments much improved the paper. Support from CRDF grant UKP2-2897-KK-07 is gratefully acknowledged. This research was also supported by the French Space Agency CNES and PNP (Programme National de Planétologie) and has benefited from the scientific environment of Paul Sabatier University (Toulouse). The authors also duly acknowledge the support of the ESA staff.

## References

- Akimov, L.A., 1975. Influence of mesorelief on the brightness distribution over a planetary disk. Soviet Astron. 19 (3), 385–388.
- Akimov, L.A., 1979. On the brightness distribution over the lunar and planetary disks. Soviet Astron. 23 (2), 231–235.
- Akimov, L.A., 1988a. Reflection of light by the Moon. 1. Kinemat. Fiz. Nebesn. Tel 4, 3–10. (In Russian).
- Akimov, L.A., 1988b. Reflection of light by the Moon. 2. Kinemat. Fiz. Nebesn. Tel 4, 10–16. (In Russian).
- Akimov, L.A., Shkuratov, Y.G., 1981. Phase-ratio distributions of the lunar surface in two spectral ranges: Preliminary studies. Astron. Tsirk. 1167, 3–6 (in Russian).
- Barabashev, N.P., 1922. Bestimmung der Erdalbedo und des Reflexionsgesetzes für die Oberfläche der Mondmeere: Theorie der Rillen. Astron. Nachr. 217, 445–452.
- Buratti, B.J., Hillier, J.K., Wang, M., 1996. The lunar opposition surge: Observation by Clementine. Icarus 124, 490–499.
- Blewett, D.T., Lucey, P.G., Hawke, B.R., Jolliff, B.L., 1997. Clementine images of the lunar sample-return stations: Refinement of FeO and TiO<sub>2</sub> mapping techniques. J. Geophys. Res. 102, 16319–16325.
- Cerroni, P., de Sanctis, M.C., Josset, J.-L., Beauvivre, S., Koschny, D., Pinet, P., Chevrel, S., Langevin, Y., Barucci, M.A., Plancke, P., Almeida, M., Hofmann, B.A., Muinonen, K., Shevchenko, V., Shkuratov, Yu., Ehrenfreund, P., Foing, B.H., 2006. Preliminary analysis of colour information from AMIE on SMART-1. Lunar Planet. Sci. XXXVII, 1831.
- Chevrel, S., Pinet, P., Head, J.W., 1999. Gruithuisen domes region: A candidate for an extended nonmare volcanism on the Moon. J. Geophys. Res. 104, 16515.
- Chevrel, S.D., Pinet, P.C., Souchon, A., Daydou, Y., Baratoux, D., Josset, J.-L., Beauvivre, S., 2008. Photometric properties of the lunar surface from AMIE/SMART-1 spot pointing observations. In: Abstract Book of Int. Conf. "Solar System Bodies: From Optics to Geology". Astronomical Institute of Kharkiv V.N. Karazin National University, Kharkiv, Ukraine, p. 24.
- Cord, A., Pinet, P.C., Daydou, Y., Chevrel, S., 2003. Planetary regolith surface analogs: Optimized determination of Hapke parameters using multi-angular spectro-imaging laboratory facility. Icarus 165, 414–427.
- Cord, A., Pinet, P.C., Daydou, Y., Chevrel, S.D., 2005. Experimental determination of the surface photometric contribution in the spectral reflectance deconvolution processes for a simulated martian crater-like regolithic target. Icarus 175 (1), 78–91.
- Cord, A., Baratoux, D., Mangold, N., Martin, P., Pinet, P., Greeley, R., Costard, F., Masson, P., Foing, B., Neukum, G., 2007. Surface roughness and geological mapping at subhектometer scale from the High Resolution Stereo Camera onboard Mars Express. Icarus 191 (1), 38–51.
- Dougnac, V., Beauvivre, S., 2008. AMIE/SMART-1 Data Processing. AMIE Sci. Meeting, Madrid, April, 10–11.
- Engelhardt, W., Hurrle, H., Luft, E., 1976. Microimpact-induced changes of textural parameters and modal composition of the lunar regolith. Proc. Lunar Sci. Conf. 7, 373–392.
- Fedorets, V.A., 1952. Photographic photometry of the lunar surface. Uchen. Zap. Khark. Univ. 42, 49–172 (in Russian).

- Foing, B.H., Racca, G.D., Marini, A., Evrard, E., Stagnaro, L., Almeida, M., Koschny, D., Frew, D., Zender, J., Heather, J., Grande, M., Huovelin, J., Keller, H.U., Nathues, A., Josset, J.-L., Malkki, A., Schmidt, W., Noci, G., Birkl, R., less, L., Sodnik, Z., McManamon, P., 2006. SMART-1 mission to the Moon: Status, first results and goals. *Adv. Space Res.* 37, 6–13.
- Foing, B.H., Koschny, D., Grieber, B., Josset, J.-L., Beauvivre, S., Grande, M., Huovelin, J., Keller, H.U., Mall, U., Nathues, A., Malkki, A., Noci, G., Sodnik, Z., Kellett, B., Pinet, P., Chevrel, S., Cerroni, P., de Sanctis, M.C., Barucci, M.A., Erard, S., Despan, D., Muinonen, K., Shevchenko, V., Shkuratov, Y., Ellouzi, M., Peters, S., Almeida, M., Frew, D., Volp, J., Heather, D., McMnamon, P., Camino, O., Racca, G., and SMART-1 STWT, 2008. SMART-1 lunar highlights. *Lunar Planet. Sci.* 39, Abstract #1987.
- Gaddis, L.R., Hawke, B.R., Robinson, M.S., Coombs, C., 2000. Compositional analyses of small lunar pyroclastic deposits using Clementine multispectral data. *J. Geophys. Res.* 105 (E2), 4245.
- Gaddis, L.R., Staid, M.I., Tyburczy, J.A., Hawke, B.R., Petro, N.E., 2003. Compositional analyses of lunar pyroclastic deposits. *Icarus* 161, 262–280.
- Gehrels, T., Coffen, T., Owings, D., 1964. Wavelength dependence of polarization. III. The lunar surface. *Astron. J.* 69, 826–852.
- Gerasimenko, S., Kaydash, V., Shkuratov, Yu., Opanasenko, N., Velikodsky, Yu., Korokhin, V., 2008. Global search for photometric anomalies of lunar nearside, 2008. In: Abstract Book of Int. Conf. "Solar System Bodies: From Optics to Geology". Astronomical Institute of Kharkiv V.N. Karazin National University, Kharkiv, Ukraine, pp. 40–41.
- Gold, T., 1971. Lunar-surface closeup stereoscopic photography. In: Apollo 14 Preliminary Science Report. NASA Spec. Publ., NASA-SP 272, pp. 239–247.
- Grieber, B., 2007. AMIE inflight dark correction. ESA technical note S1-AMIE-SGS-TN-011.
- Grieber, B., 2008. The calibration of AMIE images. ESA technical note S1-AMIE-SGS-TN-013.
- Hapke, B., 1986. Bidirectional reflectance spectroscopy. 4. Extinction and the opposition effect. *Icarus* 67, 246–280.
- Hapke, B., 1993. Theory of Reflectance and Emittance Spectroscopy. Cambridge Univ. Press, Cambridge. 450 pp.
- Hapke, B., 2001. Space weathering from Mercury to the asteroid belt. *J. Geophys. Res.* 106, 10039–10074.
- Hawke, B.R., Blewett, D.T., Lucey, P.G., Smith, G.A., Bell III, J.F., Campbell, B.A., Robinson, M.S., 2004. The origin of lunar crater rays. *Icarus* 170, 1–16.
- Helfenstein, P., Shepard, M., 1999. Submillimeter-scale topography of the lunar regolith. *Icarus* 141, 107–131.
- Jehl, A., Pinet, P., Baratoux, D., Daydou, Y., Chevrel, S., Heuripeau, F., Manaud, N., Cord, A., Rosemburg, C., Neukum, G., Gwinner, K., Scholten, F., Hoffmann, H., Roatsch, T., and the HRSC Team, 2008. Gusev photometric variability as seen from orbit by HRSC/Mars-Express. *Icarus* 197, 403–428.
- Josset, J.L., Beauvivre, S., Cerroni, P., De Sanctis, M.C., Pinet, P.C., Chevrel, S., Langevin, Y., Barucci, M.A., Plancke, P., Koschny, D., Almeida, M., Sodnik, Z., Mancuso, S., Hofmann, B.A., Muinonen, K., Shevchenko, V., Shkuratov, Yu., Ehrenfreund, P., Foing, B., 2006. Science objectives and first results from the SMART-1/AMIE Multi-Colour Micro-Camera. *Adv. Space Res.* 37 (1), 14–20.
- Kaydash, V., Kreslavsky, M., Shkuratov, Yu., Gerasimenko, S., Pinet, P., Chevrel, S., Josset, J.-L., Beauvivre, S., Almeida, M., Foing, B., 2007a. Photometric characterization of selected lunar sites by SMART-1 AMIE data. *Lunar Planet. Sci.* XXXVIII, Abstract #1535.
- Kaydash, V., Kreslavsky, M., Shkuratov, Yu., Gerasimenko, S., Pinet, P., Chevrel, S., Josset, J.-L., Beauvivre, S., Almeida, M., Foing, B., 2007b. Topography of selected lunar areas from SMART-1 AMIE data. In: Microsymposium 46. Topics in Comparative Planetology, Moscow, Russia. Abstract #M 46–34.
- Kaydash, V., Kreslavsky, M., Shkuratov, Yu., Gerasimenko, S., Pinet, P., Chevrel, S., Josset, J.-L., Beauvivre, S., Foing, B., and AMIE Smart-1 Team, 2008. The Opposition effect of the Moon from SMART-1 AMIE data. *Lunar Planet. Sci.* XXXIX, Abstract #1195.
- Koschny, D., Almeida, M., Beauvivre, S., 2003. Calibration report of the AMIE PFM, S1-AMIE-RSSD-RP-001/1a.
- Kreslavsky, M.A., Shkuratov, Y.G., 2003. Photometric anomalies of the lunar surface: Results from Clementine data. *J. Geophys. Res.* 108, doi:10.1029/2002JE001937, 5015.
- Kreslavsky, M.A., Shkuratov, Y.G., Velikodsky, Y.I., Kaydash, V.G., Stankevich, D.G., Pieters, C.M., 2000. Photometric properties of the lunar surface derived from Clementine observations. *J. Geophys. Res.* 105, 20281–20295.
- Kreslavsky, M.A., Bondarenko, N.V., Pinet, P.C., Raitala, J., Foing, B.H., Neukum, G., and Mars Express HRSC Co-Investigator Team, 2006. Mapping of photometric anomaly of martian surface with HRSC Data. *Lunar Planet. Sci.* XXXVII, Abstract #2211.
- Lucey, P.G., Blewett, D.T., Jolliff, B.L., 2000a. Lunar iron and titanium abundance algorithms based on final processing of Clementine ultraviolet-visible images. *J. Geophys. Res.* 105, 20297–20306.
- Lucey, P.G., Blewett, D.T., Taylor, G.J., Hawke, B.R., 2000b. Imaging of the lunar surface maturity. *J. Geophys. Res.* 105, 20377–20386.
- Muinonen, K., Parviainen, H., Naranen, L., Josset, J.-L., Beauvivre, S., Pinet, P., Chevrel, S., Koschny, D., Grieber, B., Foing, B., 2009. Lunar single-scattering, porosity, and surface-roughness properties with SMART-1/AMIE. *Astron. Astrophys. Lett.*, submitted for publication.
- Nozette, S., and 19 colleagues, 1994. The Clementine mission to the Moon: Scientific overview. *Science* 266, 1835–1839.
- Pieters, C., Shkuratov, Yu., Kaydash, V., Stankevich, D., Taylor, L., 2006. Lunar soil characterization consortium analyses: Pyroxene and maturity estimates derived from Clementine image data. *Icarus* 184, 83–101.
- Pieters, C.M., Head III, J.W., Isaacson, P., Petro, N., Runyon, C., Ohtake, M., Foing, B., Grande, M., 2008. Lunar international science coordination/calibration targets (L-ISCT). *Adv. Space Res.* 42, 248–258.
- Pinet, P., Shevchenko, V., Chevrel, S., Daydou, Y., Rosemberg, C., 2000. Local and regional lunar regolith characteristics at Reiner gamma formation: Optical and spectroscopic properties from Clementine and Earth-based data. *J. Geophys. Res.* 105, 9457–9475.
- Pinet, P., Cerroni, P., Josset, J.-L., Beauvivre, S., Chevrel, S., Muinonen, K., Langevin, Y., Barucci, M.A., De Sanctis, M.C., Shkuratov, Yu., Shevchenko, V., Plancke, P., Hofmann, B.A., Ehrenfreund, P., Sodnik, Z., Koschny, D., Almeida, M., Foing, B., 2005. The Advanced Moon micro-Imager Experiment (AMIE) on SMART-1: Scientific goals and expected results. *Planet. Space Sci.* 53, 1309–1318.
- Pinet, P.C., and 18 colleagues, 2006. The Mars-Express Team, MER Science Team, Mars Express/HRSC Imaging photometry and MER Spirit/PANCAM in situ spectrophotometry within Gusev. *Lunar Planet. Sci.* 37, Abstract 1220.
- Pinet, P.C., Jehl, A., Daydou, Y.D., Chevrel, S.D., Baratoux, D., Heuripeau, F., Manaud, N., Cord, A., Neukum, G., 2008. Contribution of the opposition effect to the photometric variability seen across Gusev Crater from orbit by HRSC/MARS-EXPRESS. In: Abstract Book of Int. Conf. "Solar System Bodies: From Optics to Geology". Astronomical Institute of Kharkiv V.N. Karazin National University, Kharkiv, Ukraine, pp. 99–100.
- Schlitz, P., 1976. Moon Morphology: Interpretations Based on Lunar Orbiter Photography. Univ. of Texas Press, Austin. 641 pp.
- Schlitz, P.H., Srnka, L.J., 1980. Cometary collisions on the Moon and Mercury. *Nature* 284, 22–26.
- Shkuratov, Y.G., Helfenstein, P., 2001. The opposition effect and the quasifractal structure of regolith: Theory. *Icarus* 152, 96–116.
- Shkuratov, Y., Starukhina, L., Kreslavsky, M., Opanasenko, N., Stankevich, D., Shevchenko, V., 1994. Principle of undulatory invariance in photometry of atmosphereless celestial bodies. *Icarus* 109, 168–190.
- Shkuratov, Y., Kreslavsky, M., Ovcharenko, A., Stankevich, D., Zubko, E., Pieters, C., Arnold, G., 1999. Opposition effect from Clementine data and mechanisms of backscatter. *Icarus* 141, 132–155.
- Shkuratov, Yu.G., Kreslavsky, M.A., Stankevich, D.G., Kaydash, V.G., Pinet, P., Shevchenko, V.V., Foing, B.H., Josset, J.-L., 2003. The SMART-1 Mission: Photometric Studies of the Moon with the AMIE Camera. *Solar Syst. Res.* 37 (4), 251–259.
- Shkuratov, Yu.G., Stankevich, D.G., Petrov, D.V., Pinet, P.C., Cord, A.M., Daydou, Y.H., Chevrel, S.D., 2005. Interpreting photometry of regolith-like surfaces with different topographies: Shadowing and multiple scatter. *Icarus* 173, 3–15.
- Souchon, A.L., Chevrel, S.D., Pinet, P.C., Daydou, Y.H., Shevchenko, V.V., Grieber, B., Josset, J.-L., Beauvivre, S., Shkuratov, Yu., Kaydash, V.G., and the AMIE Team, 2009. Characterization of the optical properties of J. Herschel pyroclastic deposit using SMART-1/AMIE photometric data. *Lunar Planet. Sci.* 40, Abstract #1237.
- Starukhina, L.V., Shkuratov, Yu.G., 2004. Swirls on the Moon and Mercury: Meteoroid swarm encounters as a formation mechanism. *Icarus* 167, 136–147.
- van Diggelen, J., 1964. The radiance of lunar objects near opposition. *Planet. Space Sci.* 13, 271–279.
- Wildey, R.L., 1978. The Moon in Heiligenschein. *Science* 200, 1265–1266.
- Wilhelms, D.E., 1987. The geologic history of the Moon. USGS Prof. Paper 1348.